The Magazine for Nanoscience and Technology

VOL 26 SPRING 2024

NANOscientific

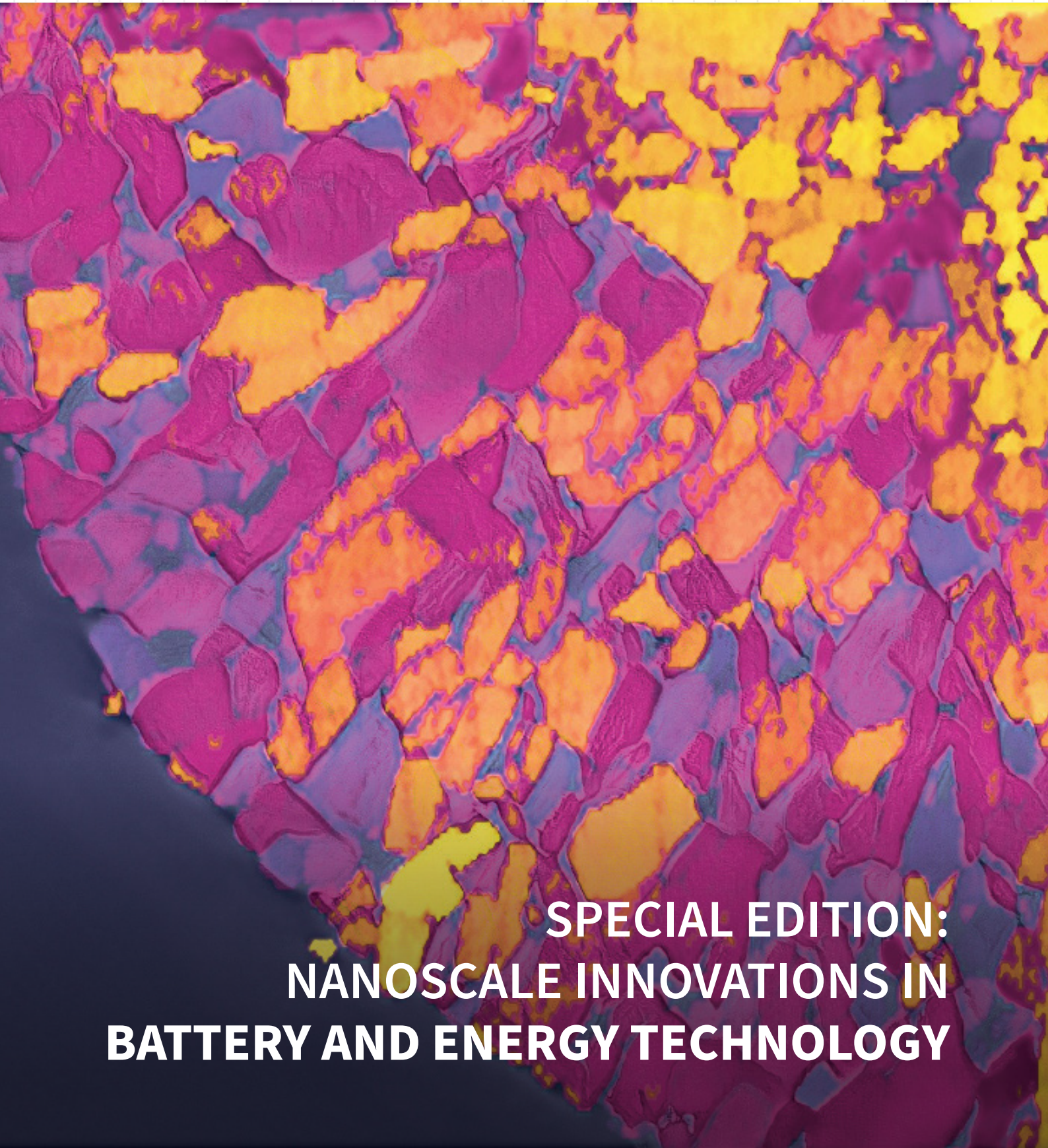

SPECIAL EDITION: NANOSCALE INNOVATIONS IN BATTERY AND ENERGY TECHNOLOGY

One Nanostep for Microscopy
One Giant Leap for Science

Park FX40

A New Class of Atomic Force Microscope: The Automatic AFM

More Information

The Park FX40 autonomously images and acquires data powered by its artificial intelligence, robotics and machine learning capability. Effortlessly, get the sharpest, clearest, highest resolution images and measurements one sample after another on various applications. Boost your progress and scientific discoveries through unprecedented speed and accuracy.

Park SYSTEMS

parksystems.com/fx40

EXPLORING THE NANOSCALE: A GLIMPSE INTO BATTERY & ENERGY TECHNOLOGY

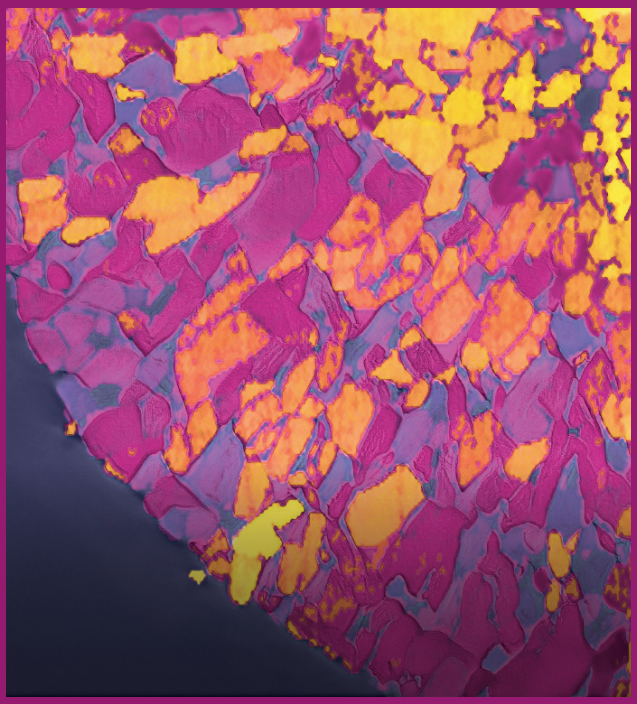

Sample: $LiNi_{0.8}Co_{0.15}Al_{0.05}O_2$ (NCA)
Mode: SSRM
Instrument: Park FX40 AFM + Glove Box

This issue features an intriguing image of $LiNi_{0.8}Co_{0.15}Al_{0.05}O_2$ (NCA), a layered nickel-based material, captured using Scanning Spreading Resistance Microscopy (SSRM). This method, a mode of Atomic Force Microscopy (AFM), reveals both the height and resistance of NCA, underscoring its potential as a cathode material for lithium-ion batteries (LIBs). The detailed SSRM image provides insight into NCA's structure and electrical properties, crucial for its application in enhancing battery technology.

INDEX

NANO scientific

- **Keibock Lee**, Editor-in-Chief
  keibock@nanoscientific.org
- **Jessica Kang**, Managing Editor
- **Sun Ham**, Editor and Point of Contact
  sun.ham@parksystems.com
- **Cathy Lee**, Technical Editor
- **Ester Cho**, Art Director

Publisher and Corporate officers
- **Sang-il Park**, Chief Executive Officer
- **Karen Cho**, EVP of Operations Management Division
- **Ryan Yoo**, EVP of Business Development
- **Sang-Joon Cho**, EVP of Research Equipment Business Unit
- **Richard Lee**, EVP of Industrial Equipment Business Unit

NanoScientific is published both in print and online to showcase advancements in the field of nanoscience and technology across a wide range of multidisciplinary areas of research. The publication is offered free to anyone who works or have interest in the field of nanotechnology, nanoscience, microscopy and other related fields of study and manufacturing.

We enjoy hearing from you, our readers.
Please send your research or story ideas to sun.ham@parksystems.com.
To view all of our articles, please visit our web site at nanoscientific.org.

ADVANCED CHARACTERIZATION OF PRISTINE CATHODES FOR LITHIUM-ION BATTERIES USING AFM: INSIGHTS FOR BATTERY RESEARCH AND DEVELOPMENT

Kylie Cha, Jake Kim, Cathy Lee
RATC, Park Systems Corp.

Introduction

Lithium-ion batteries (LIBs) are advanced portable energy storage solutions that fuel our daily devices like smartphones, laptops, and cars. To enhance their performance and quality control, we must grasp the nanoscale interaction between morphology and electronic properties. This application note introduces battery basics and how we analyze lithium-ion materials using atomic force microscopy (AFM).

A typical LIB consists of two electrodes, a separator, and an electrolyte solution (Fig. 1 [1]). During operation, electrochemical reactions occur within the electrodes, with ions moving through the electrolyte and electrons passing through an external wire, forming a closed circuit. In discharge, the anode undergoes electrochemical oxidation, while the cathode experiences reduction as chemical energy is converted into electrical energy. A separator prevents electrical shorts between the cathode and anode, and the electrolyte conducts ions but not electrons.

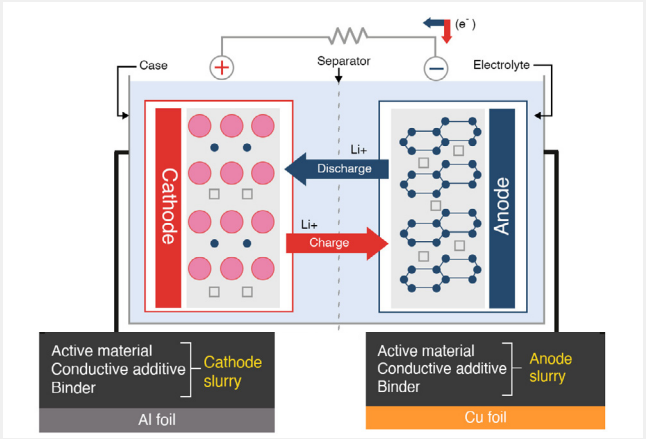

Fig. 1. Schematic of lithium-ion battery.

LIB electrodes comprise active materials, conductive materials, and binders (Fig. 2). The active material generates energy by reacting with the anode material. The cathode's material is called 'cathode active material' and it contains lithium ions. It impacts capacity and power, with materials like lithium cobalt (LCO), lithium manganese oxide (LMO), lithium cobalt aluminum (NCA), and lithium cobalt manganese (NCM) is used. The anode's material called 'anode active material' stores releases lithium ions, primarily using stable graphite. Conductive material, usually carbon black (Super-p), aids electron movement. Binders enhance material adhesion, addressing issues like battery life and charging time due to anode material volume changes during repeated cycles.

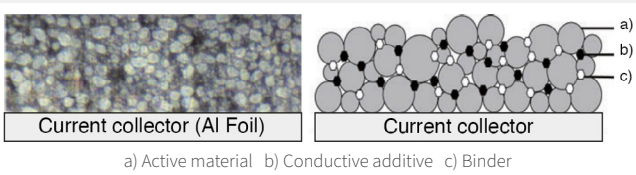

Fig. 2. Cross-sectioned pristine cathode sample (a) CCD vision image, (b) a schematic diagram.

Battery voltage and capacity depend on the active material, while LIB cycling stability relates to electrode integrity. Silicon, a promising anode material, offers ten times greater capacity than graphite [2]. Yet, silicon anodes experience substantial volume changes during charge-discharge in LIBs [3], causing stress, anode fractures, and delamination. Cathode materials also undergo structural changes, impacting functionality [4,5], leading to microcracks, increased porosity, and capacity loss during cycling. To understand LIB failure, we must study local electronic properties and morphology. This paper demonstrates AFM's ability to provide topography and work function information.

In recent years, various analytical methods such as scanning electron microscopy (SEM), transmission electron microscopy (TEM), and AFM have been extensively used in LIB research. While SEM and TEM measurements offer speed, they come with limitations in sample analysis using traditional electron beam imaging. To address this, experiments need to be conducted with diverse conditions and parameters, emphasizing the necessity for a versatile and comprehensive analytical tool.

AFM is increasingly used to study LIB electrode materials due to its micro/nano-meter spatial resolution. It assesses pristine material characteristics, aids electrode fabrication control, and investigates mechanical and electrical degradation. Surface potential measurements detect electrode degradation, including decreased cathode surface potential with more charge/discharge cycles [8]. Electrical degradation of cathode materials also leads to reduced conductivity and microcrack formation with increased cycles [6].

Park Systems introduced PinPoint™ SSRM to comprehensively characterize surface, mechanical, and electrical properties of LIB electrodes [9]. Vacuum measurements suit easily oxidizable or hydrolyzable materials like cycled electrodes.

However, for simplicity, pristine samples can be measured under ambient conditions using conventional AFMs. This paper illustrates measurements on a pristine cathode as an initial step in LIB characterization and quality assessment.

Materials and Methods

In this study, we investigated the cathode material $LiNi_{0.8}Co_{0.15}Al_{0.05}O_2$ (NCA) as a promising candidate for lithium-ion batteries (LIBs). The cathode slurry, composed of NCA, a conductive agent, and binder, was applied onto an aluminum (Al) current collector. To facilitate microscopic analysis, a cross-sectional sample was prepared using an argon-ion cross-section polisher. The Al current collector was electrically connected to the AFM's sample bias line using silver paste. Prior to AFM scanning, scanning electron microscopy (SEM) was employed to evaluate the sample's structural characteristics and microscopic uniformity.

An automated AFM system (FX40, Park Systems) was utilized, featuring advanced technology for the alignment of the super luminescent diode (SLD) beam and position-sensitive photodiode (PSPD) on the cantilever's apex. Precise beam focusing within the cantilever minimized optical interference. The incorporation of an automatic tip exchanger and laser aligner reduced labor-intensive tasks and human error. The StepScan™ function within SmartScan from Park Systems facilitated effortless configuration for automated measurements, encompassing the selection of regions of interest, imaging modes, and scan parameters.

Surface potential measurements were conducted using a conductive material-coated tip (PPP-EFM, Nanosensors) in sideband Kelvin probe force microscopy (KPFM) mode. Prior to data acquisition on the sample, we calibrated the work function of the AFM tip by referencing a freshly cleaved highly oriented pyrolytic graphite (HOPG) surface. Subsequently, scanning spreading resistance microscopy (SSRM) measurements were executed to evaluate local conductivity and resistance. A conductive diamond-coated tip (AD-40-AS, Adama Innovations) with a nominal spring constant of 40 N/m was employed to enhance electrical signal stability and minimize tip wear resulting from lateral shear forces. Measurements were conducted at three randomly selected positions on the sample to assess the uniformity of cathode fabrication. Importantly, all AFM experiments were conducted within an environmental control glove box to prevent sample deformation upon exposure to ambient air.

In Fig. 3, SEM images show the cross-sectioned cathode sample with a thickness of approximately 80 ± 10 µm (slurry thickness may vary). The cathode film is securely attached to the Al current collector. The active material particles have a uniform spherical shape and high distribution density, promoting good electrical contact and preventing current collector damage during electrode fabrication. Some minor porosity (indicated by yellow arrows) is observed, likely due to the sample fabrication method, but it's not expected to significantly affect cathode performance. SEM measurements provide an initial assessment and quality control of the electrode fabrication process by revealing the microscopic structure and uniformity.

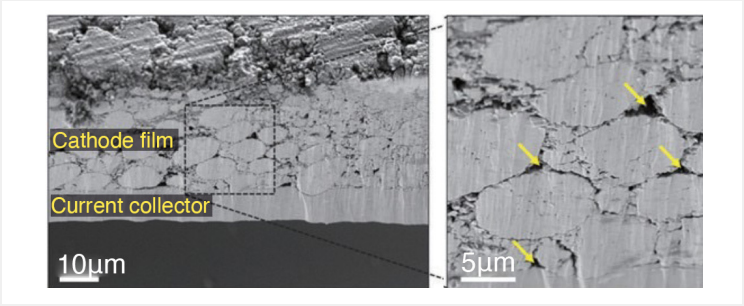

Fig. 3. SEM images obtained on cross-sectioned pristine cathode sample.

Fig. 4 reveals NCA particles' work function as 5.0 ± 0.2 eV, in line with the theoretical 4.9 eV. These KPFM results affirm the excellent state of the pristine electrode, ready for battery assembly. Furthermore, Fig. 4 highlights KPFM's ability to unveil characteristics beyond surface topography inspection.

Fig. 5 summarizes surface potential measurements at various locations using KPFM, which provides topography and surface potential simultaneously. Different AFM tips have varying work functions, leading to potential offsets.

Fig. 6 displays SSRM measurements indicating uniform conductivity across the cathode film, despite a small bias applied to the current collector, suggesting high electrical conductivity in the prepared cathode

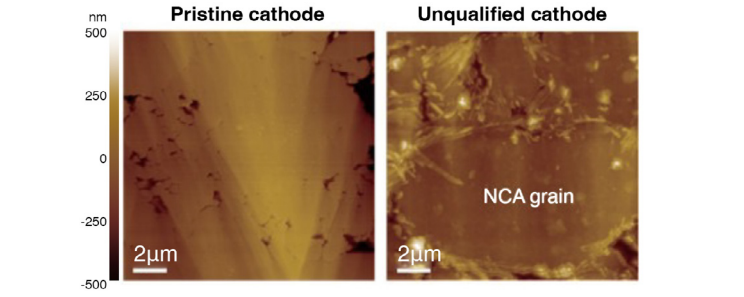

Fig. 4. Topographies of the pristine and unqualified cathode.

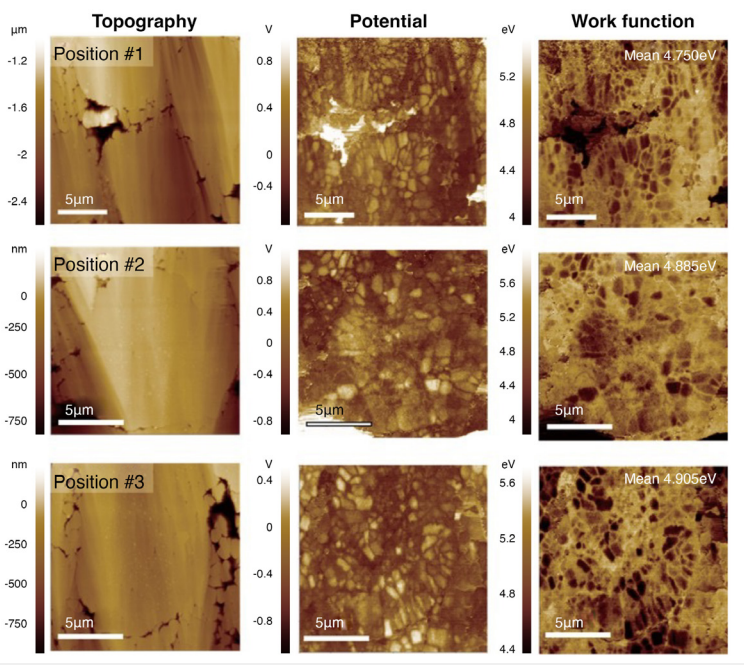

Fig. 5. KPFM results obtained at three different positions on the sample.

sample, advantageous for LIB performance. To prevent potential damage to the active material, it is advisable to use PinPoint SSRM mode for battery sample measurements, allowing simultaneous assessment of terrain, electrical, and mechanical properties while minimizing tip wear and sample damage.

Conclusion

In summary, this application note demonstrates the preparation and characterization of a pristine cathode for lithium-ion batteries (LIBs). We measured and interpreted the sample's structural, topographical, and electrical properties to enhance our understanding of the relationship between electrode characteristics and battery performance. This approach showcases the effective use of AFM for inspecting and assessing electrode quality in LIBs, paving the way for future battery research and development.

In addition to the techniques introduced here, various AFM modes offer comprehensive battery characterization capabilities, making AFM a powerful tool in battery research. These modes include:

- Conductive AFM for current distribution and conductance measurements during battery cycling.

- PinPoint electrical modes for simultaneous mechanical and electrical property measurements of electrodes.

- Electrochemical AFM for in-situ measurements of electrode surface changes during battery electrochemical processes.

- Environment control options, allowing AFM measurements in high vacuum, gases, liquids, and controlled temperature/humidity conditions.

In summary, AFM offers a versatile platform that provides nanoscale correlative information, making it invaluable tool in battery research.

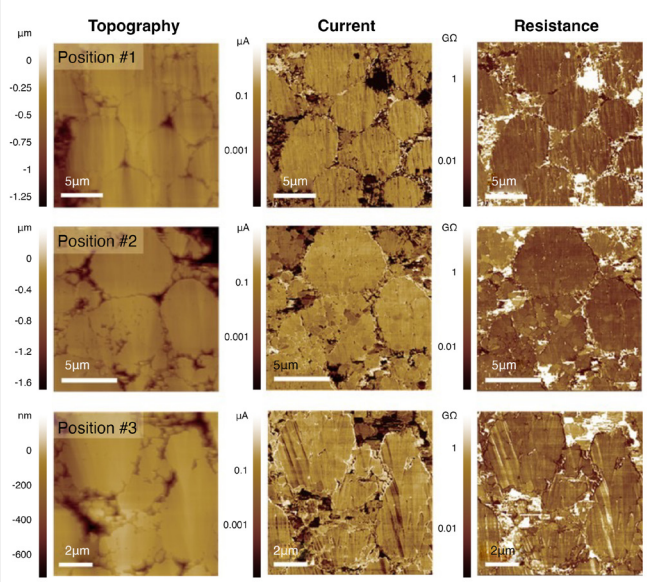

Fig. 6. SSRM results obtained at three different positions on the sample. A DC bias of 1V was applied to the current collector.

References

1. B. Goodenough, K.-S. Park, The Li-Ion Rechargeable Battery: A Perspective, J. Am. Chem. Soc. 135 (2013) 1167–1176.
2. U. Kasavajjula, C. Wang, A.J. Appleby, Nano- and bulk-silicon-based insertion anodes for lithium-ion secondary cells, J. Power Sources. 163 (2007) 1003–1039.
3. L.Y. Beaulieu, T.D. Hatchard, A. Bonakdarpour, M.D. Fleischauer, J.R. Dahn, Reaction of Li with Alloy Thin Films Studied by In Situ AFM,
J. Electrochem. Soc. 150 (2003) A1457.
4. F. Lin, I.M. Markus, D. Nordlund, T.-C. Weng, M.D. Asta, H.L. Xin, M.M. Doeff, Surface reconstruction and chemical evolution of stoichiometric layered cathode materials for lithium-ion batteries, Nat. Commun. 5 (2014) 3529.
5. J. Zheng, M. Gu, J. Xiao, P. Zuo, C. Wang, J.-G. Zhang, Corrosion/Fragmentation of Layered Composite Cathode and Related Capacity/Voltage Fading during Cycling Process, Nano Lett. 13 (2013) 3824–3830.
6. S.Y. Park, W.J. Baek, S.Y. Lee, J.A. Seo, Y.-S. Kang, M. Koh, S.H. Kim, Probing electrical degradation of cathode materials for lithium-ion batteries with nanoscale resolution, Nano Energy. 49 (2018) 1–6.
7. W. Zhao, W. Song, L.-Z. Cheong, D. Wang, H. Li, F. Besenbacher, F. Huang, C. Shen, Beyond imaging: Applications of atomic force microscopy for the study of Lithium-ion batteries, Ultramicroscopy. 204 (2019) 34–48.
8. J. Wu, S. Yang, W. Cai, Z. Bi, G. Shang, J. Yao, Multi-characterization of LiCoO2 cathode films using advanced AFM-based techniques with high resolution, Sci. Rep. 7 (2017) 11164.
9. J.P. Pineda, C. Lee, B. Kim, K. Lee, Electrical and Mechanical Characterization of Li Ion Battery Electrode using PinPoint™ SSRM, Micros. Today. 28 (2020) 48–53.
10. Park Systems Corporation, A New Class of Atomic Force Microscope: FX40, the Automatic AFM

NANOSCIENTIFIC MAGAZINE INTERVIEW

Professor Dr. Christine Kranz
Institute of Analytical and Bioanalytical Chemistry, Ulm University, Germany

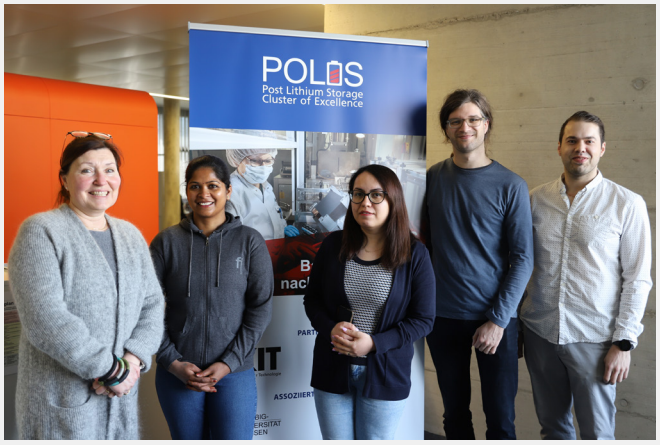

From left to right: Professor Dr. Christine Kranz, Krishanveni Palanisamy, Salimeh Saleh, Tom Philipp, and Sven Daboss of Ulm University's Institute of Analytical and Bioanalytical Chemistry in Ulm, Germany, collaboratively engage in research on post-Lithium battery interfaces.

Dr. Christine Kranz is spearheading innovative research in scanning electrochemical probe microscopy (SEPM), particularly within the realms of energy storage and conversion. A leading expert in the intricate dance of electrochemistry and nanotechnology, Dr. Kranz has adeptly combined atomic force microscopy (AFM) with scanning electrochemical microscopy (SECM) that yield not only high-resolution topographical detail but also vital electrochemical information. Her group's pioneering efforts in miniaturized amperometric sensor technology and FIB-based microfabrication have laid the groundwork for significant advancements in mapping light-driven photocatalysis and post-lithium battery research, promising to revolutionize energy storage systems.

The Kranz research team aims to unravel the complex electrochemical processes at the electrode electrolyte interface that will contribute knowledge to enable more efficient, sustainable, and cost-effective energy storage solutions. Additionally, Dr. Kranz and her team members explore scanning electrochemical cell microscopy for screening experiments of the dynamic behavior of formed interphases.

Dr. Kranz, could you share some insights into your current research at the Institute of Analytical and Bioanalytical Chemistry (IABC), Ulm University? What are the main goals and objectives of your research team?

IABC has a strong interest in instrumental analysis and instrumental development, ranging from trace element analysis to infrared spectroscopy (using QCL-based IR sensors), molecularly imprinted polymers, and in situ surface (bio) analytics. My research team focuses on developing miniaturized sensors that can be used in combination with, for example, scanning electrochemical microscopy (SECM) or hybrid AFM-SECM for applications ranging from energy-related topics to bio(medical) research. Additionally, we are interested in AFM force spectroscopy and scanning electrochemical cell microscopy (SECCM) for surface modification, for instance, for single cell studies that include bacterial cell adhesion on antimicrobial films. Regarding energy-related topics, we are engaged in multi-PI projects such as the POLiS Cluster of Excellence and the Transregio CataLight, where our research is dedicated to local in situ activity studies in light-driven molecular photocatalysis and post-Li battery research.

From a broader perspective, what do you believe will be the most significant impact of sodium-ion battery technology on the energy sector in the coming years?

Sodium-ion batteries (SIBs) are a promising alternative to traditional lithium-ion batteries (LIBs), offering future benefits such as lower cost, higher safety, and more abundant raw materials. For example, with the recent rollout of the Yiwei Sehol-E10X and JMEV EV3 in China, EVs using SIBs are already available on the market, boasting a range of about 250 km. In the context of stationary grid storage, where battery weight is less critical and low-temperature operation is advantageous, SIBs could revolutionize energy storage solutions by storing renewable energy for use during peak demand periods at low cost. Therefore, SIBs are poised to have a significant impact in the near future. However, there are still challenges, such as lower gravimetric energy density and a not yet well-established supply chain for the materials. Despite more than 40 years of LIB research, a knowledge gap still exists for SIBs.

Can you share your thoughts on the interdisciplinary nature of battery research and development and how various scientific disciplines contribute to innovations in this field?

In my opinion, battery research is inherently interdisciplinary, as it spans the entire chain from developing new electrode materials and electrolytes to gaining fundamental insights into interface processes, as well as designing and producing battery cells, and crucially, analyzing sustainability and circularity. This requires a distinctly interdisciplinary approach. Materials science, physics, and chemistry are focused on the development and characterization of new materials for cathodes, anodes, and electrolytes. In contrast, engineering is dedicated to optimizing battery design and scale-up, ensuring durability and safety. Computer science contributes through simulation and analysis. Collaborations across these disciplines, integral to the POLiS Cluster of Excellence, are vital for the sustainable advancement of battery technology and for addressing interdisciplinary challenges in developing innovative energy storage concepts.

Looking at the evolution of energy storage, how do you anticipate the role of researchers and scientists changing

as new battery technologies move from the lab to everyday applications?

Researchers are inherently flexible and able to adapt to new challenges, ensuring their work is dynamic and responsive to changing needs. Their efforts are crucial in driving the development, advancement, and integration of solutions to meet the increasing demand for sustainable energy.

Regarding your research, what inspired you to focus on the solid electrolyte interphase (SEI) in sodium-ion batteries, particularly on hard carbon (HC) composite electrodes?

The SEI layer is crucial in battery stability and performance. HC composite electrodes are mainly used as anode materials for SIBs due to their high capacity and stability. There is still a knowledge gap regarding the chemical composition and dynamics of the SEI in SIBs compared to LIBs. Therefore, it is an important aspect that sparks the interest of many research groups to understand the relevant parameters affecting the SEI and its stability during charging and discharging.

Can you discuss the benefits of ether-based electrolytes over carbonate-based ones for HC anodes in sodium-ion batteries?

Ether-based electrolytes are beneficial for their, lower viscosity, relatively low vapor pressure, and better chemical and thermal stability compared to carbonate-based electrolytes. The reduced viscosity enhances ion transport in the electrolyte, thereby boosting the rate capability and overall efficiency of SIBs. Improved electrochemical performance, such as increased coulombic efficiency and improved rate capability, has been demonstrated for HC anodes in ether-based electrolytes.

Your research includes spray-coating for HC composite electrodes. How does this technique impact the SEI compared to traditional methods?

The spray-coating technique in fabricating HC composite electrodes offers multiple advantages for laboratory-based fundamental studies compared to techniques like doctor blade coating. This method allows control over the material's thickness and the active material's mass loading on the current collector by adjusting the number of spray passes. Furthermore, it enables the creation of electrodes or coatings in various shapes needed for specific electrochemical cell applications, such as microcalorimetry or cantilever-based stress testing.

How does conductive atomic force microscopy (C-AFM) enhance the understanding of the SEI's conductivity?

C-AFM offers direct measurements of electrical conductivity at nanometer resolution, shedding light on the heterogeneity of the electrical conductivity of the SEI formed after cycling. Our C-AFM studies have examined various cycling regimes and electrolyte compositions, including additives. Comparing data from pristine and cycled samples gives important insights into the dynamic electrochemical phenomena within the SEI and their impact on conductivity. This knowledge could enable researchers to refine electrolyte formulations and create new materials to enhance battery performance and lifetime.

What unique insights have you gained from employing scanning electrochemical microscopy (SECM) alongside C-AFM?

Utilizing the Park NX10 allows for switching between C-AFM, EC-AFM, and AFM-SECM, offering the flexibility to conduct various experiments on the same sample and at the same sample positions. The SEI's primary function is to facilitate Na+ ion transport while blocking electron transport, thereby preventing further electrolyte decomposition and maintaining electrochemical reaction continuity. SECM can provide quantitative data on local electron transfer kinetics, revealing observed differences in the heterogeneous rate constant of electron transfer for pristine and cycled particles. Additionally, AFM-SECM experiments enable direct correlation of this data with the sample surface's morphological features. C-AFM is advantageous for visualizing electronic conductivity and assessing the homogeneity and electronic insulating properties of the formed interphases. In contrast, SECM yields quantitative data on electron transfer kinetics and insights into the heterogeneity and electrochemical properties of the formed layers. Analyzing the same sample both in situ (with AFM-SECM) and ex situ (using C-AFM and AFM force spectroscopy) offers a comprehensive view of the nanomechanical and electrochemical properties of the SEI.

You mention the impact of specific additives on the SEI's properties. How does this influence the battery's overall performance and longevity?

Electrolyte additives, particularly fluoroethylene carbonate (FEC), are widely utilized in lithium-ion and sodium-ion battery electrolytes to enhance performance and longevity. FEC aids in forming a stable and uniform SEI layer on the electrode surface, which helps suppress undesirable side reactions between the electrode materials and the electrolyte, thereby reducing electrolyte decomposition. This reduction in solvent decomposition enhances electrolyte stability, diminishes gas evolution, and prolongs battery life. Furthermore, FEC enhances ion transport through the SEI layer, contributing to the battery's stability and efficiency. However, it is important to note that for SIBs, findings from half-cell experiments using FEC might not directly apply to full-cell studies.

How do you foresee the role of scanning probe microscopy techniques in future research and the optimization of battery interfaces?

The field of battery research is rich with established microscopic and spectroscopic analytical techniques. However, there is growing interest in utilizing in situ scanning probe microscopy (SPM) techniques to examine interfacial processes, as traditional methods often lack spatial resolution. The high spatial resolution provided by SEPM and the ability to manipulate interfaces on the nano- to microscale, for instance, through SECCM, suggest that SPM studies may contribute to our understanding of battery interfaces. Such studies can elucidate key factors influencing battery performance, including charge transfer kinetics, ion diffusion pathways, and interface stability. It's important to note that studies on "real electrodes" might encounter artifacts, hence the potential need for model interfaces in fundamental research.

Thank you, Professor Dr. Kranz, for offering your insights and sharing your research with us.

Park FX40

The Ultimate User-Friendly Environmental Solution

Materials sensitive to environmental conditions require meticulous handling during AFM measurements to prevent property changes from exposure to oxygen and humidity. The Park FX40 Environmental Solution addresses this issue by maintaining environmental levels below 1 ppm, offering significant advantages. This integration ensures reliable and accurate measurements easily and efficiently.

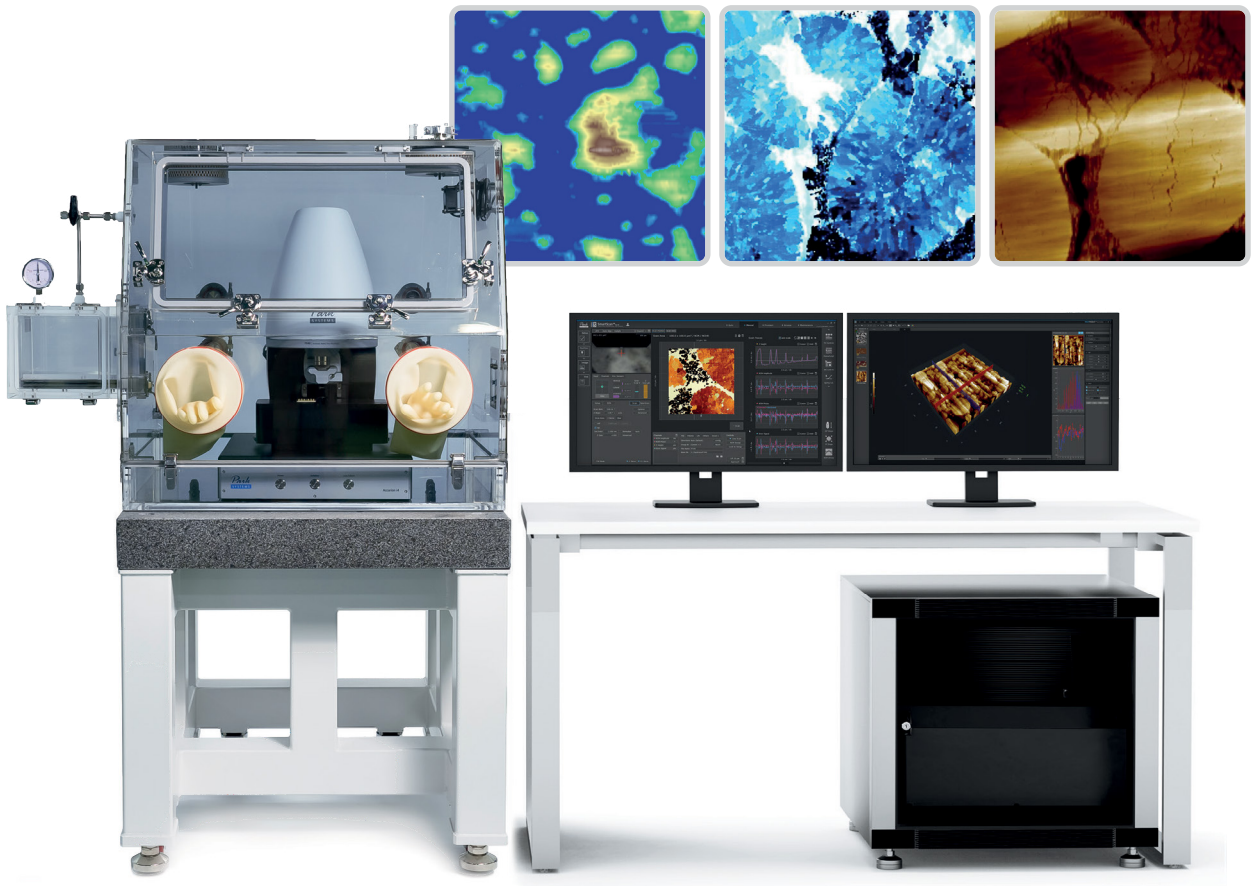

- **Ultra-Low Environmental Contamination**
  Maintains oxygen and humidity below 1 ppm, perfect for studying materials like Li-ion batteries and perovskites, safeguarding against oxidation and degradation.

- **Effortless Probe Handling**
  Includes a Probe Exchanger system for fast, easy probe swaps without inserting hands into the glovebox, thereby minimizing contamination and saving time.

- **Multi-Sample Versatility**
  Includes a Multi Sample Chuck and StepScan™ technology that allows for the sequential measurement of multiple samples and different regions, significantly boosting productivity and flexibility in experiments.

- **One-Click SLD Beam Alignment**
  Simplifies the setup process, enabling precise alignment easily and rapidly.

Park SYSTEMS

ADVANCED AFM TECHNIQUES FOR PEROVSKITE SOLAR CELL ANALYSIS AND OPTIMIZATION

Jake Kim, Kylie Cha, Cathy Lee
RATC, Park Systems Corp.

Introduction

Perovskite materials show promise for use in photovoltaic cells, devices that convert light into electricity efficiently and cost-effectively, potentially replacing traditional silicon-based solar cells. These cells typically consist of a thin perovskite layer between two electrodes, where light generates electron-hole pairs collected by the electrodes to produce electric current [1]. The key advantage of perovskite solar cells is their rapidly increasing efficiency, reaching a reported record of 26% in a decade [2]. Additionally, their cost-effective manufacturing makes them a viable option for large-scale deployment.

In this application note, we showcase Atomic Force Microscopy (AFM) modes including Kelvin Probe Force Microscopy (KPFM), Conductive AFM (C-AFM), and Photo Current Mapping (PCM) for perovskite material analysis. Experiments are performed in a glove box for accuracy due to perovskite's sensitivity to temperature and humidity [3]. Control of oxygen and humidity levels is crucial for precise measurements. Park Systems's environmental system (Park NX GloveBox with gas purification) achieves low water and oxygen concentrations (<35 ppm) [3].

KPFM and C-AFM

KPFM and C-AFM are two techniques for studying materials. KPFM is a non-contact surface imaging method that measures surface potential with high spatial resolution. In the context of perovskites, KPFM helps analyze surface potential variations, work function, and built-in potential of the solar cell layers, offering insights into energy level alignment [4], [5]. Fig. 2 displays sideband KPFM results, offering superior spatial resolution compared to Amplitude Modulation (AM)-KPFM. It's primarily influenced by the AFM tip apex, detecting electrostatic force gradient through frequency changes for better resolution. These results reveal local surface potential variations, indicating regions with different electronic properties linked to charge carrier concentration and perovskite material composition, morphology, or defects.

C-AFM, a contact mode imaging technique, measures nanoscale electrical conductivity. It is valuable for studying the local conductivity of the perovskite layer, shedding light on charge transport properties. By mapping perovskite layer conductivity, C-AFM aids in understanding charge transport mechanisms and optimizing perovskite solar cell performance [6], [7]. Fig. 3 demonstrates C-AFM, where a conductive AFM tip scans the perovskite film surface while applying 0.5 V to the bottom layer. The surface current image reveals localized regions of slightly higher or lower conductivity under red light (635 nm), suggesting varying carrier concentrations within the perovskite film.

Oxygen and Moisture Level	< 35 ppm (with NX Glove box)
Measuring Sensor Range	• Oxygen: 0 - 1000 ppm • Moisture: 0 - 500 ppm
Automatic Pressure Control Range	-15 to +15 mbar
Working Gas	Nitrogen (N_2), Argon (Ar) or Helium (He)
Box Purging System	Automatic Control
Filter	1-filter column gas purifier

Fig. 1. Park Systems NX GloveBox with gas purification system setup and its specifications.

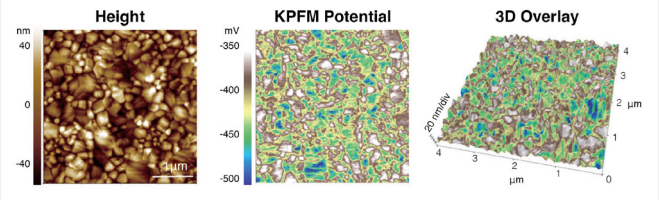

Fig. 2. KPFM results (Height, KPFM potential and 3D Overlay (Overlaying the KPFM potential information in the height image) images) on perovskite thin film. Scan size: 4 μm×4 μm, pixel: 512×256, performed by Park NX10.

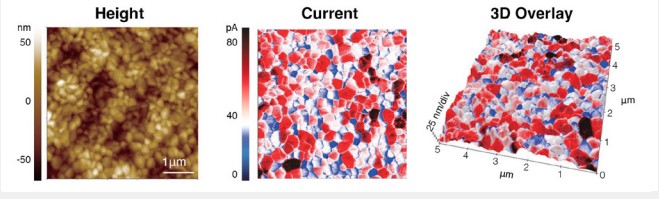

Fig. 3. C-AFM results (Height and current images) on perovskite thin film. Scan size: 5 μm×5 μm, pixel size: 512×512, performed by Park NX10. Image courtesy: Kanjanaboos Lab, Mahidol University, Thailand

Observing the photoelectric effect

The photovoltaic effect describes the absorption of light within a semiconductor which promotes an electron from the valence band into the conduction band. In the case of perovskite solar cells, this means that such photo-excited electrons and the remaining positively charged “hole” in the valence band populate a higher energy level within the semiconductor with increased mobility. Accordingly, these charge carriers can migrate through the semiconductor until they reach either the boundary of the perovskite layer or recombine. If the perovskite is sandwiched between two charge-selective layers, where one only allows electrons to pass and the other only allows holes to pass, then the respective cell has rectifying properties and the charge carriers can be collected on either side of this layered structure to harness electric energy [8]. Experimentally, the photovoltaic effect can be studied on a single perovskite layer by illuminating the semiconductor and measuring the local conductance. Since the concentration of free charge carriers increases upon illumination, the measured conductance also increases.

The photovoltaic effect involves light absorption in a semiconductor, promoting an electron from the valence band to the conduction band. In perovskite solar cells, this results in photo-excited electrons and positively charged "holes" in higher energy levels with enhanced mobility. These charge carriers can move through the semiconductor until they either reach the perovskite layer's boundary or recombine. When the perovskite is between two charge-selective layers, one permitting only electrons and the other only holes to pass, the cell exhibits rectifying properties. Charge carriers can be collected on either side of this layered structure to generate electric energy [8]. Experimentally, the photovoltaic effect can be studied in a single perovskite layer by illuminating the semiconductor and measuring local conductance. As the concentration of free charge carriers increases with illumination, the measured conductance also rises.

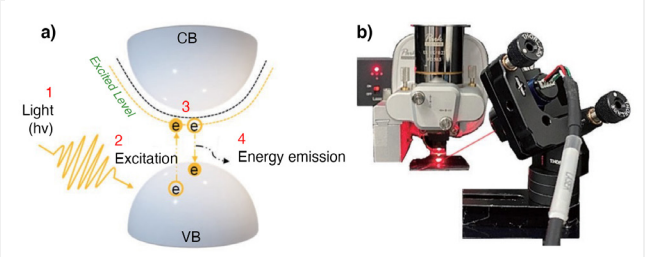

Fig. 4. Schematic of photovoltaic effect, 1. Light source exposure, 2. Excitation of electron, 3. Electron-hole pair combination, 4. Energy emission of electron (a), Park Systems PCM module, applicable light source: red (Wavelength of 635 nm), blue (405 nm), IR (785 nm) (b).

Park Systems provides an optimal setup for investigating the photovoltaic effect using external laser and sample bias (Fig. 4b). Applicable types of light sources are red (Wavelength of 635 nm), blue (405 nm), infrared (IR, 785 nm) of external lasers, and internal LED (White source, 400 ~ 750 nm) and SLD (830 nm). On/off control for external laser and SLD, 0~100 % (Adjustable unit 0.1%) intensity control for LED is possible. The light source and sample bias are controlled as synced parameter by SmartScan™ (AFM operation software, Park Systems). General PCM measurement process is mainly three steps, 1. Reset bias (A+B in Fig. 5), 2. Applied bias with light driving (C in Fig. 5), 3. Resting (F-A+B+C in Fig. 5). The reset bias serves to neutralize any remaining charges in the measurement area. Sufficient time is required for the current to stabilize. Applied bias and the light source of time duration can be specified by the user so that spectroscopy of photovoltaic reaction is measured as current variation through time (Fig. 5).

Park Systems offers an ideal setup for studying the photovoltaic effect using external lasers and sample bias (Fig. 4b). Various light sources, including red, blue, and infrared external lasers, as well as internal LED and SLD, are available. Users can control laser and SLD on/off and adjust LED intensity from 0% to 100% (in 0.1% increments). SmartScan™ synchronizes light source and sample bias control.

The PCM measurement process involves three steps:

1. Reset bias (A+B in Fig.5) to neutralize remaining charges.
2. Apply bias with controlled light exposure (C in Fig. 5).
3. Measure current variation over time to study the photovoltaic reaction.

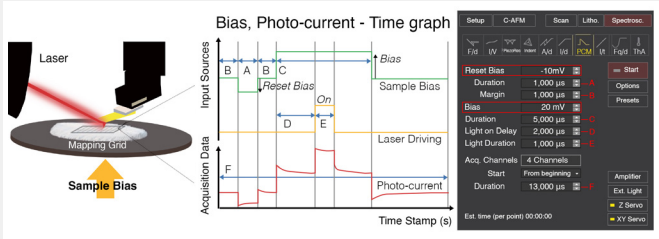

Fig. 5. Park Systems’ PCM operation process and related parameters

Fig. 6 shows measurements of the electrical properties of a formamidinium lead iodide ($FAPbI_3$) film using KPFM and C-AFM. To investigate the photovoltaic effect, the LED light intensity was adjusted, and the electrical properties were measured (KPFM; Potential and Work function, C-AFM; Current) with respect to the light intensity. $FAPbI_3$ is a type of hybrid organic-inorganic perovskite material that has been widely investigated for use in photovoltaic solar cells. It has properties that allow for efficient light absorption and charge transport, making it a promising candidate for next-generation solar cell technology. As mentioned above, when perovskite materials absorb light, they generate free charge carriers (electrons and holes), which can then be separated and collected as electrical current. The electrical properties of perovskite materials are strongly influenced by the intensity of light absorption. As the intensity of LED increases, more free charge carriers are generated, leading to an increase in the electrical current that can be extracted from the material. In KPFM images, changes in potential and work function according to the intensity of light can be confirmed. As the intensity of light increases, the contrast does not appear clearly due to saturation. The C-AFM image also shows a similar trend to that of KPFM, but a clearer contrast is identified in each step. Typically, perovskite solar cells exhibit a nonlinear response to changes in light intensity [9]. At low light intensities, the current generated by the cells is proportional to the light intensity. However, at higher light intensities, the current saturates and becomes independent of further increases in light intensity. This nonlinear response is attributed to a combination of factors, including the limited diffusion length of charge carriers, which can lead to recombination and loss of charge carriers at high light intensities, and the finite lifetime of the charge carriers, which limits the amount of charge that can

be collected before recombination occurs.

Fig. 6 displays electrical property measurements of a formamidinium lead iodide ($FAPbI_3$) film using KPFM and C-AFM. To investigate the photovoltaic effect, LED light intensity was adjusted, and properties (KPFM: Potential and Work function, C-AFM: Current) were measured relative to light intensity. $FAPbI_3$, a hybrid organic-inorganic perovskite, is promising for solar cells due to efficient light absorption and charge transport. Light absorption in perovskites generates charge carriers (electrons and holes) that impact electrical properties. Higher LED intensity results in more charge carriers and increased electrical current extraction. KPFM shows potential and work function changes but may saturate with high light intensity. C-AFM exhibits a similar trend with clearer contrast. Perovskite solar cells exhibit nonlinear responses to light intensity changes. At low intensities, current is proportional, but at higher intensities, it saturates due to charge carrier limitations and recombination [9].

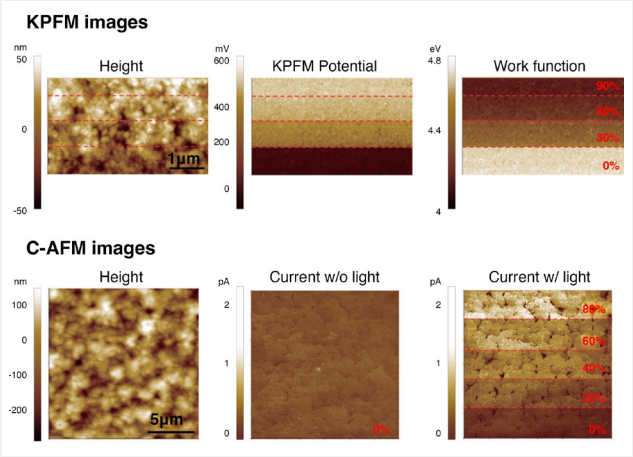

Fig.6. Changes in electrical properties according to light intensity of perovskite thin film, measured by KPFM and C-AFM. Red fonts indicate induced light intensity. Scan size: 5 μm×4 μm, pixel size: 512×256 for KPFM, scan size: 15 μm×15 μm, pixel size: 512×256 for C-AFM, performed by Park NX10.

Conclusion

Perovskite solar cells offer significant potential as cost-effective, highly efficient alternatives to traditional silicon solar cells. Realizing this potential requires access to suitable methods, equipment, and controlled environments for material analysis and performance enhancement. AFM, particularly KPFM and C-AFM, proves invaluable for investigating diverse aspects of perovskite materials.

Furthermore, the C-AFM setup, when equipped with an external laser module, enables time-resolved exploration of photoconductive properties using our PCM technique. PCM provides insights into photo-decay processes, shedding light on recombination and trap density within photo absorbers. By correlating high-resolution data on surface potential and conductivity of the perovskite layer with topographical information, these techniques aid researchers in optimizing perovskite solar cell performance and developing more efficient and durable solar cell technologies.

Lastly, Park Systems offers an optimal research environment for perovskite and perovskite solar cells, granting precise control over parameters like temperature and humidity. This control significantly facilitates future research on this material, contributing to its advancement and widespread application in solar cell technology.

References

1. Jung, H. S., & Park, N. G. (2015). Perovskite solar cells: from materials to devices. small, 11(1), 10-25.
2. https://www.nrel.gov/pv/interactive-cell-efficiency.html
3. Yun, J. S., Kim, J., Young, T., Patterson, R. J., Kim, D., Seidel, J., ... & Ho-Baillie, A. (2018). Humidity-induced degradation via grain boundaries of HC (NH2) 2PbI3 planar perovskite solar cells. Advanced Functional Materials, 28(11), 1705363.
4. Kang, Z., Si, H., Shi, M., Xu, C., Fan, W., Ma, S., ... & Zhang, Y. (2019). Kelvin probe force microscopy for perovskite solar cells. Sci. China Mater, 62(6), 776-789.
5. Bergmann, V. W., Weber, S. A., Javier Ramos, F., Nazeeruddin, M. K., Grätzel, M., Li, D., & Berger, R. (2014).
Real-space observation of unbalanced charge distribution inside a perovskite-sensitized solar cell. Nature communications, 5(1), 5001.
6. Si, H., Zhang, S., Ma, S., Xiong, Z., Kausar, A., Liao, Q., ... & Zhang, Y. (2020). Emerging conductive atomic force microscopy for metal halide perovskite materials and solar cells. Advanced Energy Materials, 10(10), 1903922.
7. Leblebici, S., Leppert, L., Li, Y. et al. (2016). Facet-dependent photovoltaic efficiency variations in single grains of hybrid halide perovskite. Nat Energy 1, 16093.
8. Kayesh, M. E., Chowdhury, T. H., Matsuishi, K., Kaneko, R., Kazaoui, S., Lee, J. J., ... & Islam, A. (2018). Enhanced photovoltaic performance of FASnI3-based perovskite solar cells with hydrazinium chloride coadditive. ACS Energy Letters, 3(7), 1584-1589.
9. Glowienka, D., & Galagan, Y. (2022). Light intensity analysis of photovoltaic parameters for perovskite solar cells. Advanced Materials, 34(2), 2105920.

REAL-TIME IMAGING OF NA⁺ REVERSIBLE INTERCALATION IN "JANUS" GRAPHENE STACKS FOR BATTERY APPLICATIONS

Jinhua Sun[1], Matthew Sadd[2], Philip Edenborg[3], Henrik Grönbeck[3], Peter H. Thiesen[4], Zhenyuan Xia[1], Vanesa Quintano[5], Ren Qiu[6], Aleksandar Matic[2], Vincenzo Palermo[1,5*]

[1]Materials and Manufacture, Chalmers University of Technology, Göteborg, Sweden (CU of T). [2]Materials Physics, Dep. of Physics, (CU of T). [3]Dep. of Physics, CU of T. [4]Accurion GmbH, Göttingen, Germany. [5]Institute of Organic Synthesis and Photoreactivity, National Research Council of Italy, Bologna, Italy. [6]Microstructure Physics, CU of T. *vincenzo.palermo@isof.cnr.it

This study introduces "Janus" graphene, a novel material with one-sided functionalized graphene sheets, enabling reversible sodium (Na^+) intercalation, a key for sodium-ion batteries. Using operando Raman spectroelectrochemistry and imaging ellipsometry, the research demonstrates Janus graphene's effective Na^+ storage, comparable to graphite in lithium-ion batteries. The material's design, featuring uniform pores and controlled functionalization, along with theoretical insights into its Na^+-NH_2 interaction, highlights its potential in advancing sodium-ion battery technology.

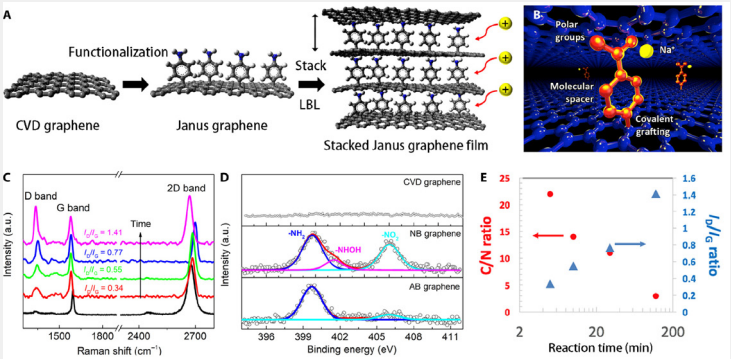

Fig. 1 Preparation of Janus graphene. A. Illustration depicting the creation of Janus graphene and its assembly into thin films. B. Representation of Na^+ ions inserted between graphene layers separated by AB spacers. C. Graph showing variations in AB graphene's functionalization density through extended reaction with 4-NBD. D. XPS spectral comparison highlighting nitrogen peaks across CVD, NB, and AB graphene samples, with noted x-ray induced conversion from -NO_2 to -NH_2. E. Trend showing the C/N ratio decline and I_D/I_G ratio rise in correspondence with prolonged reaction times.

INTRODUCTION

Lithium ions exhibit high loading and specific capacity in graphite, forming binary graphite intercalation compounds essential for current batteries [1–3]. In contrast, sodium ions achieve lower loadings and capacity in graphite, with limitations partly attributed to graphite's small interlayer distance [4–8]. Despite sodium's potential as a cost-effective and abundant alternative to lithium, its intercalation is hindered, unlike larger potassium ions or solvated sodium ions, which can intercalate, albeit with drawbacks like significant volume changes and reduced capacity [9–14]. Developing sodium-ion batteries (SIBs) necessitates bare sodium ion intercalation, akin to lithium in existing batteries. Sodium's intercalation challenges relate to its lower ionization potential and larger ionic radius compared to other alkali metals, affecting its electrostatic interaction with graphene [15–18]. We introduce a novel "Janus" graphene, a nanostructured material with one-sided functionalization allowing controlled sodium intercalation, monitored via operando Raman spectroelectrochemistry and imaging ellipsometry, and supported by density functional theory (DFT) calculations (Fig. 1A).

RESULTS

Synthesis of Janus Graphene. We synthesized Janus graphene from high-quality graphene monolayers using chemical vapor deposition (CVD), followed by functionalization with 4-nitrobenzene diazonium tetrafluoroborate (4-NBD) (Fig. 1A). This process, involving aryl radical formation, allows controlled grafting of molecules to graphene, with the ability to adjust the grafting density by altering reaction conditions. Post-grafting, the nitrobenzene groups were converted to aminobenzene groups, creating two graphene variants with different surface chemistries but identical functionalization densities. Characterization techniques like Raman spectroscopy, cyclic voltammetry, and X-ray photoelectron spectroscopy confirmed the grafting and subsequent chemical conversion (Fig. 1, C to E). Notably, the introduction of functional groups increased hydrophilicity, as shown by reduced water contact angles for the modified graphene. Raman analysis revealed the formation of sp^3 hybridization and covalent bonding, with an observable shift in the 2D band related to the interaction and separation of graphene layers influenced by functionalization density. The optimal Na^+ storage was achieved with an intermediate functionalization level, minimizing self-polymerization and ensuring efficient sodium storage capabilities.

Preparation of Stacked Janus Graphene Films Via Supramolecular Interactions. After synthesizing Janus graphene, we developed a method to stack layers without the typical PMMA residue issues, enhancing ion intercalation. Our approach involved using a PMMA graphene bilayer to collect floating graphene layers post-copper substrate etching (Fig. 1A), enabling the construction of a clean, multi-layered structure (Fig. 2A). Raman mapping distinguished the overlapping layers, with an I_G/I_{2D} ratio indicative of the reduced interaction between layers due to AB molecules acting as spacers, confirmed by AFM and TEM (Figs. 2B-D). The measured stacking distances, larger than in pristine graphene, suggest AB molecules align perpendicularly between layers, a structure conducive to Na^+ ion intercalation, as explored through computational methods.

DFT Analysis of Na^+ Intercalation in Janus Graphene. DFT calculations were employed to explore the optimal arrangement of AB and NB molecules within graphene layers and to assess the energetics of Na^+ and Li^+

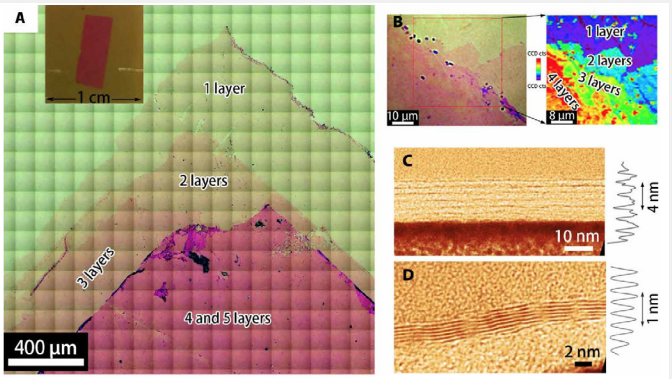

Fig. 2. Stacked AB Graphene Multilayer Analysis: A. Optical microscopy reveals the layered edge structure of AB graphene with a macro view inset displaying the sample on a silicon wafer. B. Detailed Raman intensity mapping of AB graphene's 2D band corresponds with the optical imagery. C-D. TEM cross-sections exhibit the contrasting structures of AB graphene and CVD graphene stacks, with intensity profiles alongside.

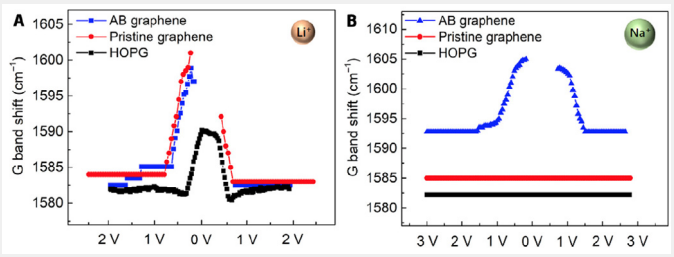

Fig. 3. Li^+ vs. Na^+ Intercalation in Various Materials: A. G band shifts indicating Li^+ intercalation observed in HOPG, graphene, and AB graphene. B. Na^+ experiments reveal no intercalation in HOPG or graphene, but successful intercalation in AB graphene. Data near 0 V omitted due to excessive G band diminishment affecting measurement accuracy.

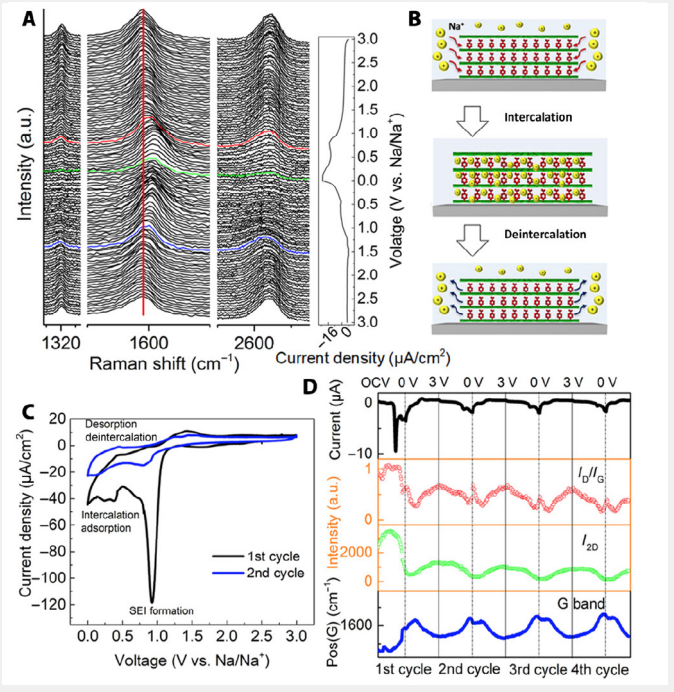

Fig. 4. Operando Raman Tracking of Na^+ in AB Graphene: A. Raman spectra show Na^+ intercalation/deintercalation at various voltages; notable shifts at 0.6 V (red), 0.05 V (green), and 1.5 V (blue) against Na^+/Na, with corresponding current on the right. B. Illustrative depiction of the intercalation process. C. CV profiles over initial cycles indicate SEI formation via a diminishing cathodic peak at a sweep rate of 0.042 mV/s. D. Graphs displaying reversible shifts in current, I_D/I_G ratio, 2D band intensity (I_{2D}), and G band position with cycling potential.

intercalation. The calculations supported a vertical orientation of molecules acting as spacers, aligning with AFM data. Na^+ was found to intercalate most effectively when coordinated with the -NH_2 group of AB and positioned in a graphene hollow site, enhancing stability through a synergistic effect. Charge density analysis indicated significant charge transfer, facilitating Na^+ interaction with graphene and AB. Various configurations were analyzed, demonstrating the highest stability when Na^+ is near the -NH_2 group, with energy barriers low enough to allow Na^+ diffusion within the material. This suggests efficient Na^+ storage in AB-functionalized graphene, with potential for high Na^+ coverage while maintaining energy stability.

Operando Raman Spectroelectrochemistry for Na^+ Intercalation in Janus Graphene. Utilizing the uniformity of Janus graphene, we monitored Na^+ and Li^+ intercalation/deintercalation via operando Raman spectroscopy, cyclic voltammetry (CV), and imaging ellipsometry (IES). Initial tests on standard materials confirmed Li^+ intercalation through a G band shift, while Na^+ showed no shift in graphite or pristine graphene but did in AB graphene stacks (Fig. 3A, 3B). The G band shift in AB graphene indicated direct Na^+ intercalation, with optimal intercalation observed at an I_D/I_G ratio between 0.5 and 0.8, balancing electrical conductivity and active site availability. Unlike Li^+ in graphite, Na^+ intercalation in AB graphene was direct, without stages, suggesting uniform intercalation across all layers. Initial cycles showed a low coulombic efficiency due to solid electrolyte interphase (SEI) formation, stabilizing after the first cycle (Fig. 4C). Operando Raman revealed changes in band intensity correlating with Na^+ intercalation levels, which were reversible and indicative of stable Na^+ storage. XPS post-discharge confirmed Na+ intercalation, with a high estimated storage capacity significantly surpassing that of graphite, attributed to the material's large interlayer distance and active sites (Fig. 4D). The findings highlight Janus graphene's unique capacity for Na^+ intercalation, not mirrored in materials like reduced graphene oxide.

Visualization of Na^+ Intercalation in Janus Graphene Using Operando IES. Operando imaging ellipsometry (IES) was utilized to microscopically observe Na^+ intercalation in AB graphene films. The technique's sensitivity to refractive index and layer thickness changes was evident in the Δ and Ψ angle variations, directly linked to Na^+ intercalation, as shown by color transitions in microscopic maps and consistent with CV data (Fig. 5). Increased optical density from Na^+ accumulation between layers suggested alterations in the material's optoelectronic properties. To corroborate these observations, we employed Park Systems Accurion's optical modeling software (nanofilm_EP4) for a simplified simulation, reflecting the impact of Na^+ on the ellipsometric angles Δ. The simulation, while qualitative, aligned with the experimental data, attributing the observed IES changes to refractive index variations due to Na^+ integration within the graphene layers. This macroscopic visualization indicated intercalation starting predominantly from the sample edges, highlighting Janus graphene's integrity and its edge-minimized design compared to more disordered materials, facilitating a nuanced understanding of Na^+ interaction within the material.

DISCUSSION

The unique structure of Janus graphene, with functionalization on only one surface, offers distinct advantages over symmetrically functionalized graphene. This asymmetric

Microscopic Thin Film Metrology and Visualization

Empower your research with our next-generation Imaging Ellipsometer

Accurion EP4

The Accurion EP4 is our latest generation of imaging ellipsometers that combines ellipsometry and microscopy. This enables the characterization of thickness and refractive index with the sensitivity of ellipsometry on micro-structures as small as 1 μm. The microscopic part enables a simultaneous measurement of all structures inside the field of view of the optical system.

- High lateral ellipsometric resolution for thickness and refractive index on microstructures as small as 1 μm.
- Intuitive region selection through drawing in the live ellipsometric view before measurement.
- Continuous spectroscopic imaging ellipsometry from UV to NIR.
- Expanded application of ellipsometry to small structures with new features and accessories.

Park SYSTEMS

parksystems.com/ep4

functionalization leads to better alignment in stacked layers due to reduced interlayer interaction, enabling a deeper understanding of Na^+ intercalation in graphite-based materials. Janus graphene's uniform pore size and minimal edges, resulting from using large-scale CVD graphene sheets, contribute to its superior Na^+ stabilization compared to pristine graphite, as shown by DFT calculations. Unlike Li^+ in crystalline graphite, Na^+ in Janus graphene undergoes direct stage 1 intercalation without intermediate stages, challenging the classical intercalation model. This behavior, distinct from that in disordered carbons like reduced graphene oxide, is influenced by the presence of AB molecules, facilitating Na^+ intercalation not observed in pristine graphene. The AB molecules not only act as spacers but also have a synergistic effect with graphene to stabilize Na^+ ions, as corroborated by DFT studies and operando experiments (Raman, CV, IES) during SIB charging/discharging processes.
These findings highlight Janus graphene's potential in SIB applications, demonstrating how asymmetric functionalization can enhance ion storage and stability, offering a new perspective for developing advanced graphite-based materials for energy storage.

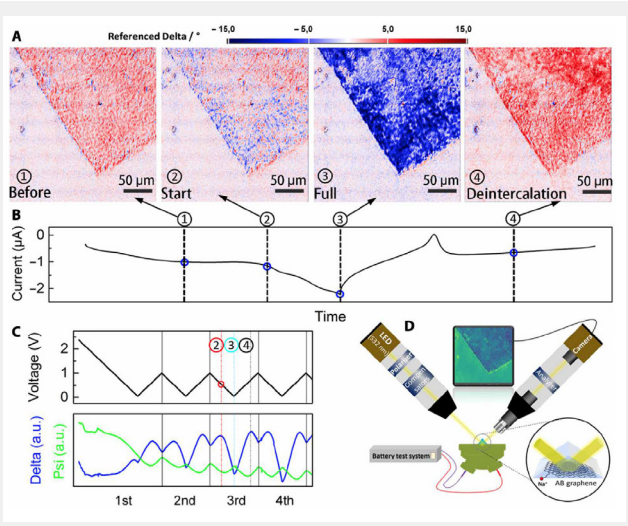

Fig. 5. IES Analysis of Na^+ in Janus Graphene: A. IES-generated maps show ellipsometric angle Δ variations during Na^+ movement in AB graphene. B. The current-time profile corresponding to the Na^+ intercalation/deintercalation. C. Fluctuations in voltage, Δ, and Ψ angles tracked across the intercalation/deintercalation cycle. D. Diagram of the IES experimental configuration.

MATERIALS AND METHODS

Synthesis of NB-functionalized CVD Graphene: CVD graphene was sourced from Graphenea, Spain, and 4-NBD from Sigma-Aldrich or synthesized as per protocol [43]. Functionalization involved immersing graphene in 4-NBD solutions of varying concentrations with sodium dodecyl sulfate for improved solubility. The immersion time varied to control NB group density, followed by extensive washing. Functionalization was selectively done on the top surface, preserving the bottom surface attached to the copper, which was later etched away without affecting the bottom graphene layer.

Electrochemical Conversion to AB Groups: The NB groups were electrochemically reduced to AB groups in a KCl and water/ethanol solution, monitored via CV curves, with a significant reduction peak indicating successful conversion. This process used a three-electrode system, cycling the material from −0.3 to −1.3 V, showing almost complete conversion after the first cycle, followed by thorough rinsing.

Assembly of Single-Graphene Sheets to Prepare Stacked Multilayers: We developed an alternative graphene transfer method to avoid PMMA contamination, using a single PMMA coating on the first graphene layer and then "fishing" additional layers from water after copper etching. This method allowed for the assembly of multiple graphene layers without PMMA residues. The functionalization increased graphene's hydrophilicity, improving layer alignment and stack quality, evidenced by AFM imaging, in contrast to the poor stacking of non-functionalized graphene. This technique ensures better interlayer sliding and high-quality multilayer graphene films, suitable for various substrates and Raman characterization.

Stacking CVD Graphene to Prepare Pristine CVD Graphene Thin Film: Pristine CVD graphene films were stacked using a modified Janus graphene method, adjusting water's surface tension with isopropanol for flatness.

Materials Characterization
IES analysis utilized an IES analysis was conducted with a Park Systems Accurion EP4 system in a polarizer compensator sample analyzer (PCSA) configuration. Unlike traditional ellipsometers, this setup includes an objective and a charge-coupled device (CCD) camera, enabling imaging capabilities. The EP4 features a monochromator that delivers monochromatic light across a broad wavelength spectrum, ranging from 250 to 1700 nm, allowing for versatile material characterization. Material characterizations included XPS (PHI 5500), Raman, TEM, and AFM for surface and thickness analysis. Contact angles were measured using a Theta meter.

Raman spectroelectrochemical characterization was performed with an EL-CELL Raman cell, employing graphene stack working electrodes and lithium and sodium counter electrodes for LIBs and SIBs. Electrolytes of 1 M $LiPF_6$ in EC/DEC and 1 M $NaPF_6$ in EC/DMC were utilized, with nickel foil for electrical contacts, and a 632-nm laser for targeting the Janus graphene electrode. Na^+ intercalation/deintercalation was facilitated by CV, Raman-monitored at 20-minute intervals, and capacity was inferred from the fourth cycle's cathodic peak.

DFT calculations, using VASP and PBE with D3 correction, analyzed intercalation energies, optimized graphene lattice constants, and studied interlayer distances, revealing preferred configurations for Li and Na intercalation. Charge transfer analysis indicated ionic bonding between Na and graphene, with charge localization near the cation.

Operando IES explored Na^+ intercalation dynamics in Janus graphene with a nanofilm_EP4 setup from Park Systems Accurion GmbH, featuring a high-resolution CCD camera and LED light source. Microscopic maps at a 45° incidence angle and 1 µm ellipsometric resolution were recorded, illustrating the sensitivity of IES to Na^+ intercalation and providing insights into ion transport mechanisms, crucial for optimizing battery material performance.

SUPPLEMENTARY MATERIALS, REFERENCES AND NOTES

Supplementary material, references and notes for this article is available at http://advances.sciencemag.org/cgi/content/full/7/22/eabf0812/DC1

SURFACE PROPERTIES-PERFORMANCE RELATIONSHIP OF ALUMINUM FOIL AS NEGATIVE ELECTRODE FOR RECHARGEABLE ALUMINUM BATTERIES

Noha Sabi,*[a, b] Krishnaveni Palanisamy,[c] Fatemehsadat Rahide,[a] Sven Daboss, [c] Christine Kranz,[c] and Sonia Dsoke*[a]

[a] Prof. Dr. N. Sabi, F. Rahide, Prof. Dr. S. Dsoke Institute for Applied Materials (IAM) Karlsruhe Institute of Technology (KIT), Germany noha.sabi@um6p.ma sonia.dsoke@kit.edu [b] Prof. Dr. N. Sabi High Throughput Multidisciplinary Research (HTMR) Mohammed VI Polytechnic University, Morocco [c] K. Palanisamy, Dr. S. Daboss, Prof. Dr. C. Kranz Institute of Analytical and Bioanalytical Chemistry Ulm University, Germany

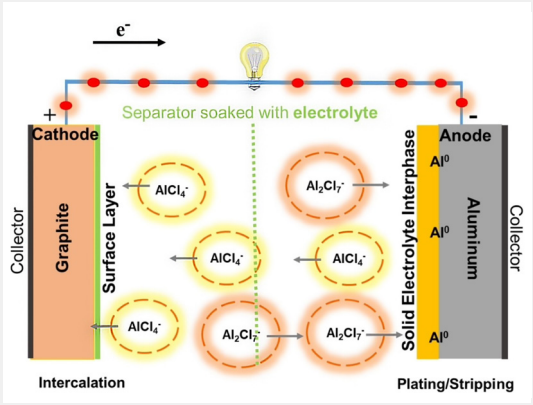

Charging principle of an Al battery using graphite as intercalating positive electrode and Al metal as the negative electrode with $AlCl_3$/EMImCl as the electrolyte (molar ratio of 1.5/1).

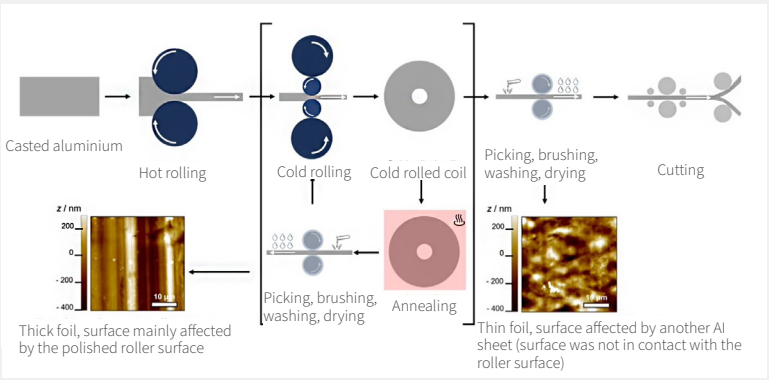

Simplified scheme of the main manufacturing processes of rolled aluminum and how the process can affect its surface finishing.

Abstract

Rechargeable aluminum batteries are gaining attention due to aluminum's abundance and stability. Understanding how initial surface properties of aluminum electrodes affect battery performance is crucial. We investigate the impact of aluminum foil surface properties on electrochemical behavior in half-cells. Different thicknesses (from 0.025 to 0.1 mm) of commercial aluminum foils with the same purity and hardness show varying microstructures and surface roughness, affecting cyclability. Atomic force microscopy (AFM) reveals corrosion of aluminum foil after cycling, leading to cell failure. The 0.075 mm thickness exhibits the best cycling stability.

Introduction

The rising demand for lithium-ion batteries (LIBs) has spurred interest in alternative energy storage systems utilizing more abundant resources. Rechargeable aluminum batteries (RABs), leveraging aluminum as the negative electrode material, offer promising theoretical capacity and sustainability. Unlike lithium and cobalt, aluminum is abundant and readily recyclable, making it an attractive option for future energy storage systems.

Aluminum boasts high gravimetric and volumetric capacities compared to other metals used in batteries, but it faces challenges with acidic ionic liquid-based electrolytes. Efficient plating and stripping depend on achieving a specific molar ratio between $AlCl_3$ and the ionic liquid to enable crucial electrode processes.

Positive electrode materials in aluminum batteries employ intercalation or conversion mechanisms, with examples including vanadium oxide for intercalation and aluminum-sulfur batteries for conversion. Despite aluminum's favorable properties, issues such as self-consumption and foil degradation persist, necessitating the use of acidic electrolytes to enhance plating/stripping.

Surface properties of aluminum foils, including purity, thickness, and roughness, significantly impact electrochemical performance but are often overlooked. The production process influences surface morphology, with factors like rolling methods and cleaning techniques affecting grain composition and coating.

Through AFM, SEM, and XRD analyses, we examine aluminum foils with identical purity but varying thicknesses, correlating these properties with electrochemical performance. This study sheds light on the crucial role of foil stability during long-term cycling in $AlCl_3$/EMImCl electrolyte under accelerated aging conditions.

Results and Discussion

Microstructural characterization of Al foils

Microscopic techniques (AFM and SEM) were utilized to examine the surface finishing of pristine aluminum foils labeled as Alx (with x = 0.1,

0.075, 0.06, 0.05, 0.04, and 0.025, representing thickness in mm). AFM images (Fig. 1) were obtained from three distinct areas of each sample without prior surface cleaning or etching. SEM images in Fig. 2 display the microstructure of the pristine foils, revealing varied surface microstructures with rolling artifacts and grain boundaries observed in thicker foils (Al0.1 and Al0.075). In contrast, thinner foils (Al0.06, Al0.05, Al0.04, and Al0.025) exhibit less pronounced rolling artifacts and narrower spacing between stripes, consistent with AFM findings. XRD patterns confirm these observations, indicating variations in microstructure among the foils. These results underscore that foil structure and surface properties differ depending on the manufacturing process, irrespective of purity.

Electrochemical characterization via cyclic voltammetry

Electrochemical characterization via cyclic voltammetry reveals significant insights into the behavior of Al foils. Initially, minimal current densities are observed due to the presence of an Al_2O_3 layer, hindering ionic pathways. Plating/stripping current densities sharply increase from the 5th cycle, indicating passivation layer dissolution. A shift in oxidation peak intensity suggests foil corrosion and increased polarization over cycles. Plating/stripping capacities and coulombic efficiencies vary among foils, with Al0.075 demonstrating stable capacities and good efficiency. Cycling performances at a higher scan rate of 20 mV/s show sharp capacity increases until stabilization, with Al0.075 exhibiting the highest capacities. These variations suggest differing deposition morphologies and dendrite distributions, influencing the overall cycling performance.

Ex-situ characterization of the aluminum foils

Ex-situ characterization via AFM (Fig. 3) and XRD reveals significant insights into the behavior of aluminum foils after cyclic voltammetry. AFM analysis after 10 cycles shows altered morphology, with granular features in Al0.025 and Al0.05 and cracks in Al0.06 and Al0.1. Surprisingly, Al0.075 exhibits the least fractured microstructure. After 100 cycles, all samples show a granular microstructure due to Al deposition, with surface changes unrelated to thickness but influenced by surface roughness and microstructure. XRD patterns indicate a decrease in the intensity of the 111 reflection, particularly noticeable in Al0.025, corresponding to the formation of a new surface observed in AFM.

Accelerated aging by cycling at high temperature

Accelerated aging through high temperature cycling significantly impacts foil stability. SEM images after 100 cycles reveal foil dissolution and consumption (Fig. 4). Cyclic voltammetry at 60 °C and 80 °C initially shows higher current densities due to decreased electrolyte density and viscosity. However, foil degradation occurs rapidly, with Al0.025 failing after 12 cycles, and Al0.04 and Al0.05 deteriorating completely after 28 cycles. Plating/stripping capacities at 60 °C display low coulombic efficiency, improving slightly after 10 cycles but remaining unstable. Increasing to 80 °C enhances capacities but accelerates degradation, with foils lasting only a few cycles. The first cycle at elevated temperatures shows increased plating/stripping current densities, indicating accelerated stripping due to aluminum oxidation.

Effect of the electrolyte/electrode contact on the foils' microstructure

Two tests were conducted to determine the primary influence on the films' microstructure: immersing Al foils for durations equivalent to 10 (6 hours) and 100 (18 hours) cycles at 10 mV/s. AFM (Fig. 5) and SEM (Fig. 6) analyses showed minor changes

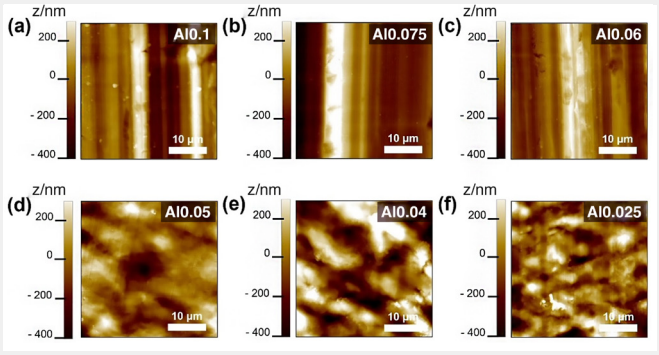

Fig. 1. AFM topography images of the different pristine Al foils.

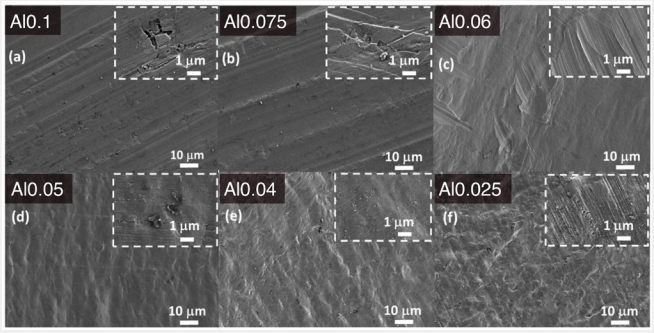

Fig. 2. SEM images of the different pristine Al foils.

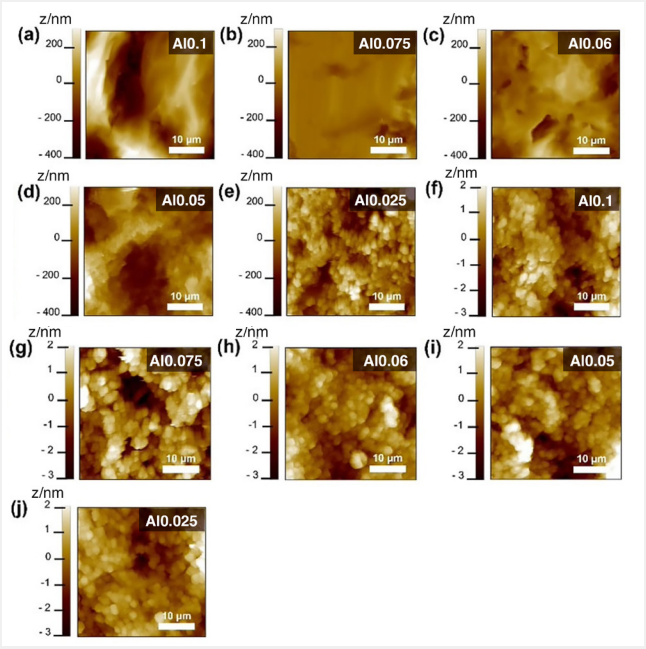

Fig. 3. AFM topography images (30Å~30 µm) of Al foils. a–e) Al foils cycled 10Å~ and f–j) Al foils cycled 100Å~ (in $AlCl_3$/EMImCl electrolyte).

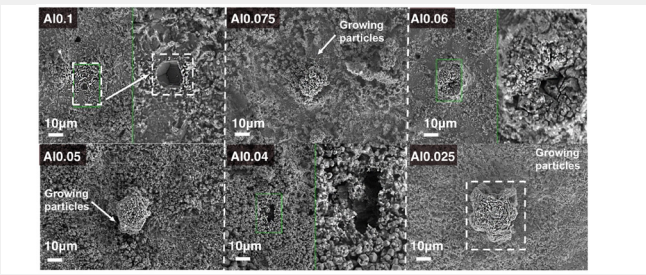

Fig. 4. SEM images of Al foils after 100 CV cycles in $AlCl_3$/EMImCl (1.5/1).

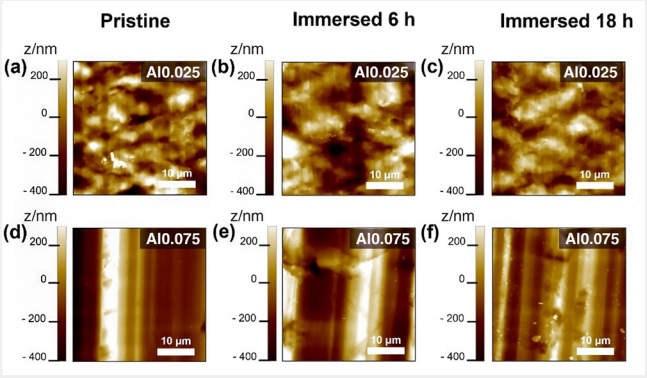

Fig. 5. AFM images (30 µm×30 µm) of: a) Al0.025 (pristine), b) Al0.025 6 h, and c) Al0.025 18 h immersion time in $AlCl_3$/EMImCl electrolyte. d) Al0.075 (pristine), e) Al0.075 6 h and f) 18 h immersion time in $AlCl_3$/EMImCl electrolyte.

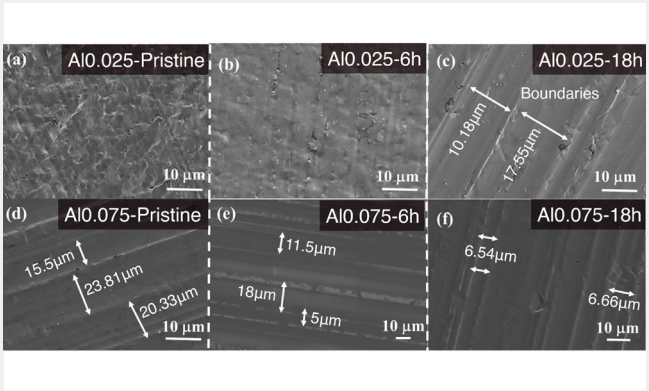

Fig. 6. SEM images of the Al0.075 and Al0.025, a and d) as received, b and e) 6 h immersed, c and f) 18 h immersed in $AlCl_3$/EMImCl (1.5/1), respectively.

in surface morphology for Al0.025 and decreased roughness for Al0.075 after immersion. XRD patterns revealed more significant changes in crystallographic orientations for Al0.025 compared to Al0.075 after immersion, suggesting greater sensitivity to electrolyte exposure. The results indicate that surface roughness increases during cycling due to corrosion and deposition, while static conditions lead to decreased roughness, possibly from native Al_2O_3 layer dissolution and new passivation layer formation. Foils with lower surface roughness perform better, while those with grain boundaries, like Al0.025, exhibit instability and microstructural changes, even with electrolyte contact.

Experimental Section

Materials and chemicals

Electrolyte Preparation

The IL-based electrolyte was prepared in an argon-filled glovebox with controlled humidity. $AlCl_3$ (anhydrous, Sigma Aldrich, 99.99%) was slowly added to EMImCl (Sigma Aldrich, ≥95%) at a molar ratio of 1.5/1 ($AlCl_3$/EMImCl) while stirring at room temperature, resulting in a yellowish viscous liquid. Aluminum foils with various thicknesses (0.025 mm, 0.04 mm, 0.05 mm, 0.06 mm, 0.075 mm, and 0.1 mm) were obtained from Goodfellow (purity: 99%, temper: annealed). After 10 and 100 cycles, the cells were disassembled in the glovebox. The excess electrolyte was removed by rinsing each foil three times with acetonitrile (anhydrous, Sigma Aldrich, 99.8%), followed by vacuum drying for one hour to remove any residual acetonitrile.

Characterization of the pristine and cycled Al foils

X-ray diffraction (XRD) analysis used a STOE STADI P diffractometer with Mo Kα1 radiation in rotating transmission mode. Aluminum foils were covered with kapton film under argon. Microstructural examination utilized a Zeiss Supra 55 Scanning Electron Microscope (SEM) with a 15 keV primary electron beam, where samples were mounted on a steel holder using carbon sticky tape.

AFM measurements on both pristine and cycled Al foils were conducted using an AFM microscope (Park NX10, Park Systems) within a glovebox under an Ar atmosphere (MBraun, O_2, H_2O < 0.1 ppm). Morphological changes and roughness were assessed before and after 10 and 100 cycles in $AlCl_3$/EMImCl electrolyte, covering foil thicknesses from 0.025 to 0.1 mm. High aspect ratio silicon AFM probes (PPP-NCHR, NanoWorld AG) with a 330 kHz resonant frequency and 10 nm tip radius were utilized. Images were captured at 0.7 Hz scan speed. The force constant (k = 42 N/m) was determined via the thermal noise method. Roughness analysis (Sa, arithmetic roughness) employed an imaging processing tool (XEI 5.2, Park Systems) at three spots (30 µm×30 µm, n = 3). Statistical analysis included two-tailed nonparametric Mann-Whitney U tests with a significance level of p = 0.05. Results showed no statistically significant difference for 0.025 mm Al foils, while a significant difference was observed for 0.075 mm Al foils.

Electrochemical measurements

Electrochemical tests were conducted using a Biologic potentiostat/galvanostat (Biologic VMP13) at temperatures of 25 °C, 60 °C, and 80 °C, covering a voltage range of 0.5–2.0 V (vs. Al) at scan rates of 10 mV/s or 20 mV/s. High scan rates were chosen to match the performance of Al/graphite systems to electrochemical supercapacitors in terms of power density. Cyclic voltammetry tests were performed using a TSC surface cell from rhd instruments (Germany) configured as a three-electrode airtight system.

Conclusions

This study investigated how surface properties of commercial aluminum foils, characterized using AFM and XRD, influence their electrochemical behavior in an $AlCl_3$/EMImCl IL-based electrolyte. AFM measurements reveal different surface roughness of the as-received foils. Foils with higher surface roughness, such as Al0.025 and Al0.05, showed instability and rapid degradation during cycling, while Al0.075, with lower surface roughness and preferred crystal orientation (200), performed the best. These findings underscore the importance of considering surface roughness, crystal orientation, and foil thickness when selecting aluminum foils for stable electrochemical performance.

PRIMER: THE ADVANCEMENTS AND APPLICATIONS OF SCANNING SPREADING RESISTANCE MICROSCOPY (SSRM)

Introduction

To advance the fields of semiconductor device technology and energy storage solutions, various analytical methods have been established. Among these, Scanning Spreading Resistance Microscopy (SSRM) is gaining recognition for its effectiveness in analyzing the electrical properties of semiconductors and batteries. SSRM, operating under the principles of Scanning Probe Microscopy (SPM), employs a tip coated with a conductive material that traverses a surface—be it semiconductor, metal, or battery material—with an applied electrical bias. This innovative approach allows the tip to measure key electrical properties such as current, conductance, and resistance, providing insights into the microscale electrical behaviors of these materials. Particularly noteworthy is SSRM's capacity to use a logarithmic amplifier, enabling the assessment of a broad range of materials from insulators to metals. This capability is pivotal not only in enhancing the performance and reliability of semiconductor devices but also in advancing our understanding of battery materials, contributing to the development of more efficient and durable energy storage systems.

Technical Challenges and Solutions

A common challenge with semiconductor and metal surfaces is that they can form an insulating oxide layer when exposed to the atmosphere. To obtain accurate resistance measurements, SSRM ensures an ohmic (unrestricted) contact by removing this oxide layer, thus allowing direct contact with the underlying material. This is achieved using a robust diamond-coated AFM (Atomic Force Microscopy) tip. For precise measurements, a significant force is applied between the tip and the sample to penetrate any oxide or contamination layer. Moreover, performing SSRM measurements in a controlled environment like a vacuum or under a nitrogen atmosphere is advised to prevent the sample surface from undergoing re-oxidation or moisture adsorption during the analysis process.

SSRM vs. SRP: Comparative Analysis

For the purpose of assessing a wide range of resistances within semiconductor devices, which typically consist of layers of metal, semiconductor, and oxide with resistances spanning from ohms to giga ohms, the use of a logarithmic current amplifier is crucial. This is due to the fact that a linear current amplifier is limited to a small current range determined by its gain setting. Scanning Spreading Resistance Microscopy (SSRM) is a refined adaptation of the traditional Spreading Resistance Profiling (SRP) method, applied at the micro and nanoscale to cross-sectioned samples.

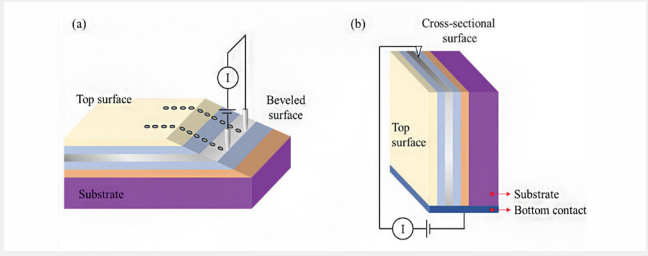

Fig. 1. Schematic diagrams of (a) SRP and (b) SSRM

Unlike the conventional SRP that relies on a dual probe system with probes around 1 µm in radius, SSRM employs an AFM tip with a much smaller radius of only a few tens of nanometers, scanning narrowly defined regions of the device. This is depicted in Fig. 1, which contrasts the SRP and SSRM setups. SSRM, avoiding the carrier dispersion issues associated with beveled surfaces in SRP, measures resistance between a back-contact and the AFM tip along a cross-sectional surface. The calculation of resistance follows Ohm's law (R = V/I), with the spatial resolution hinging on the tip's radius of curvature. The precision in resistance measurements relies heavily on minimizing contact resistance, which can be achieved by applying greater force between the tip and the sample. To ensure an optimal Ohmic contact, SSRM requires not only a high contact force but also a contaminant-free sample surface and stable environmental conditions. Accordingly, an AFM probe designed with a stiff lever and a robust tip is recommended to perform accurate SSRM measurements.

In a typical setting, current flows throughout the entire area of a sample. However, with SSRM, when the sample is engaged with a sharp AFM tip, it allows for the detection of current spread in the immediate vicinity of the tip, due to the small contact area. This is illustrated in Fig. 2(b). The formula for spreading resistance in an ideal scenario is RS = ρ/4a, where ρ represents the local resistivity of the sample and a stands for the contact area, which is influenced by the radius of the AFM tip.

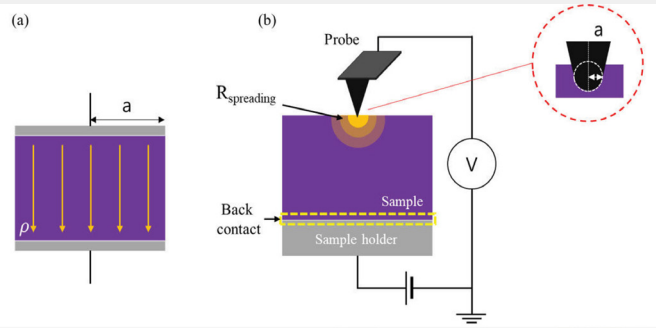

Fig. 2 illustrates two schematic representations: (a) shows the typical current flow between two parallel metal plates, and (b) depicts the spreading of current at the point of contact between the AFM (Atomic Force Microscopy) tip and the back-contact of the sample.

The surface texture of the sample plays a significant role in these measurements. A rough surface can alter the actual contact area between the AFM tip and the sample, complicating the task of obtaining precise resistance values. To counter this, sample preparation through polishing to smooth the surface, followed by cleaning to remove any residue, is essential. This process ensures the acquisition of accurate doping profiles. Fig. 3(a) presents the equipment used for polishing cross-sectional samples, while Fig. 3(b) and Fig. 3(c) depict optical images of sample surfaces, demonstrating the difference between insufficient and sufficient polishing, respectively.

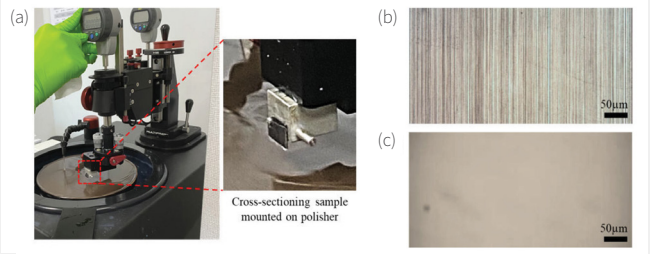

Fig. 3 displays: (a) a polisher used for preparing cross-sectioned samples; (b) an optical camera view of a sample surface that has been inadequately polished; and (c) an optical camera view of a sample surface that has been polished to a satisfactory level.

Methodology and Precision in SSRM Measurements

Establishing an ohmic contact between the scanning tip and the sample is crucial in SSRM because the presence of an oxide layer can significantly increase contact resistance. This increase can lead to a Schottky-barrier formation, which would result in inaccurate resistance readings. Fig. 4 illustrates the process of the scanning tip traversing the sample's surface, during which it removes the oxide layer, thereby effectively reducing the contact resistance as shown in Fig. 4(a). The corresponding line profile in Fig. 4(b) displays how the resistance measured at the surface varies in response to different amounts of force applied to the tip.

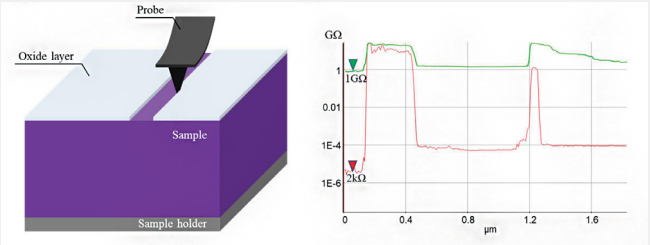

Fig. 4 depicts: (a) a diagrammatic representation of an SSRM measurement process where the tip traverses the sample to strip away the insulating oxide layer on the surface; (b) a comparison of line profiles illustrating the measured resistance at the oxide layer when subjected to high loading force (indicated in red) versus low loading force (indicated in green).

Case Studies and Applications

In an experimental demonstration, an IFX dopant calibration sample, known as the "NP20" provided by Infineon, was examined using SSRM with a sample bias of 1.5 V_DC. This particular sample was structured with 20 distinct doping conditions, featuring regions of phosphorus-doped n-type and boron-doped p-type areas on a silicon substrate. The resultant SSRM resistance image, Fig. 5(a), along with the line profile depicted in Fig. 5(b) highlight the variance in resistance across the array of doped states. These variations were captured using a logarithmic current amplifier, which is capable of spanning the entire dynamic resistance range of the sample, from the lowest to the highest resistances presented by the different dopant states.

Conclusion

In summary, Scanning Spreading Resistance Microscopy (SSRM) serves as a vital tool for the precise electrical analysis of semiconductor devices. SSRM's capability to penetrate insulating layers and measure resistance across a broad range of conductivities enhances its utility in the semiconductor industry. Critical factors for its success include the need for a clean sample surface and controlled environmental conditions to ensure accuracy. The technique's application to both semiconductor calibration and lithium-ion battery analysis highlights its versatility and potential impact on the development of advanced electronic materials and energy storage solutions. SSRM thus represents a significant stride forward in nanoscale material characterization.

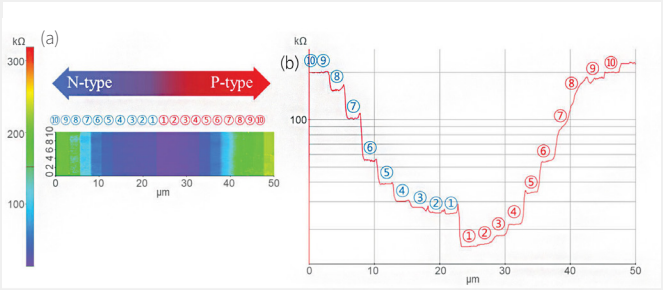

Fig. 5 presents: (a) an image illustrating the resistance mapping obtained through SSRM; (b) a line profile analysis of the IFX dopant calibration sample known as "NP20," featuring 20 distinct implanted regions of n-type and p-type on a silicon substrate, assessed with a 1.5 V_DC bias.

(c)

P doped surface (n type)	Concentration (/cm³)	B doped surface (p type)	Concentration (/cm³)
1	1.5×10^{20}	1	1.0×10^{21}
2	5.5×10^{19}	2	8.0×10^{19}
3	1.2×10^{19}	3	1.4×10^{19}
4	5.0×10^{18}	4	5.0×10^{18}
5	1.0×10^{18}	5	1.2×10^{18}
6	4.0×10^{17}	6	3.0×10^{17}
7	1.0×10^{17}	7	1.0×10^{17}
8	4.0×10^{16}	8	4.0×10^{16}
9	1.0×10^{16}	9	1.0×10^{16}
10	4.0×10^{15}	10	4.0×10^{15}

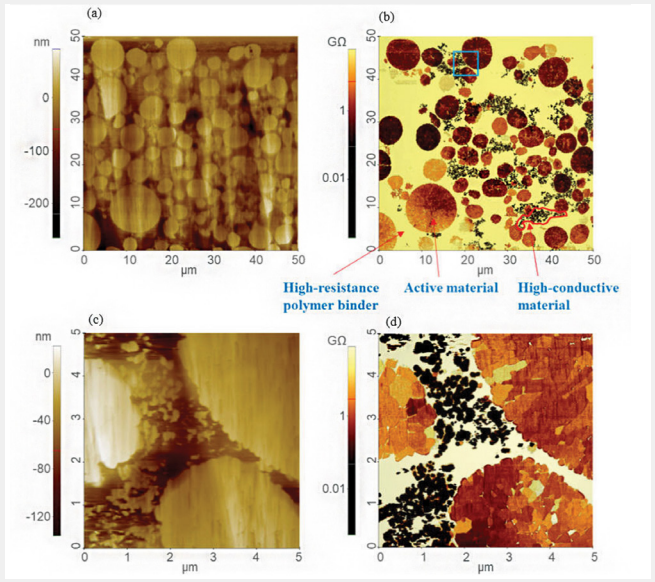

Fig. 6 illustrates the SSRM analysis conducted on the cathode surface of a rechargeable lithium-ion battery. These batteries are commonly utilized across various devices, including laptops, mobile phones, tablets, and vehicles. Given the sensitivity of lithium-ion batteries to environmental conditions, particularly humidity and nitrogen exposure, stringent controls are necessary during handling to avoid potential damage. For the measurements depicted, the sample was placed in a vacuum environment using the NX-Hivac system to ensure stability. The resulting SSRM images detail the distribution of electrical resistance across different components, such as highly conductive materials, polymer binders, and the active materials within the battery. This distribution is clearly delineated in the visual data provided by Figs. 6 (b) and (d).

PHOTOCHEMICALLY DRIVEN SOLID ELECTROLYTE INTERPHASE FOR EXTREMELY FAST-CHARGING LITHIUM-ION BATTERIES

Minsung Baek[1], Jinyoung Kim[1], Jaegyu Jin[2] & Jang Wook Choi[1,3]

[1] School of Chemical and Biological Engineering and Institute of Chemical Processes, Seoul National University, Seoul, Republic of Korea. [2] Institute of Battery Technology, SK on, Daejeon, Republic of Korea. [3] Department of Materials Science and Engineering, Seoul National University, Seoul, Republic of Korea. jangwookchoi@snu.ac.kr

This article has been condensed from Nature Communications volume 12, Article number 6807 by NanoScientific under a Creative Commons Attribution 4.0 International License for the purpose of providing shorter and more accessible reading. For the full original article, please go to https://doi.org/10.1038/s41467-021-27095-w.

ABSTRACT

Extremely fast charging (i.e. 80% of storage capacity within 15 min) is a pressing requirement for current lithium-ion battery technology and also affects the planning of charging infrastructure. Accelerating lithium ion transport through the solid-electrolyte interphase (SEI) is a major obstacle in boosting charging rate; in turn, limited kinetics at the SEI layer negatively affect the cycle life and battery safety as a result of lithium metal plating on the electrode surface. Here, we report a γ-ray-driven SEI layer that allows a battery cell to be charged to 80% capacity in 10.8 min as determined for a graphite full-cell with a capacity of 2.6 mAh cm^{-2}. This exceptional charging performance is attributed to the lithium fluoride-rich SEI induced by salt-dominant decomposition via γ-ray irradiation. This study highlights the potential of non-electrochemical approaches to adjust the SEI composition toward fast charging and long-term stability, two parameters that are difficult to improve simultaneously in typical electrochemical processes owing to the trade-off relation.

INTRODUCTION

Lithium-ion batteries (LIBs) have revolutionized technology with significant impacts on electronics and electric vehicles, where the solid–electrolyte interphase (SEI) is crucial for battery performance, affecting lithium ion movement and overall battery longevity[1,2,3,4,5,6,7,8].

Fast charging is essential for electric vehicle (EV) users, challenging due to the interfacial resistance at the anode, which affects battery safety and life by causing lithium metal plating; hence, enhancing SEI stability is vital[7,9,10].

SEI engineering, traditionally reliant on electrolyte additives, now explores γ-ray irradiation to refine SEI composition, providing a novel approach to control the SEI's inorganic and organic balance more precisely[11,12,13,14,15,16,17,18].

Utilizing γ-ray-induced SEI layers on graphite anodes demonstrated a significant reduction in charging time to 10.8 minutes for 80% capacity, showcasing a promising method for achieving rapid charging without compromising battery durability.

RESULTS

Electrochemical vs. photochemical SEI

Electron transfer in electrochemical and photochemical solid-electrolyte interphase (SEI) formation is depicted in Fig. 1a, showing unidirectional electron movement from graphite to electrolytes in the electrochemical process, resulting in indiscriminate decomposition of electrolyte components. In contrast, γ-ray-driven photochemical reactions can selectively decompose compounds, especially fluorine (F)-containing salts, due to their propensity to form stable radicals, as illustrated in Fig. 1b, enhancing SEI tunability[19,20,21,22]. This process favors the formation of lithium fluoride (LiF), enhancing fast charging by forming an inorganic-rich SEI layer[23,24].

X-ray photoelectron spectroscopy (XPS) analysis compared the compositions of electrochemically and photochemically created SEI layers (echem-SEI and photo-SEI) using the same electrolyte, revealing distinct differences. The echem-SEI showed a mix of organic and inorganic components, while the photo-SEI, produced by irradiating a graphite electrode in electrolyte with γ-rays, was significantly richer in inorganic components, as evidenced by the presence of $LiPF_6$, LixPFy, and LiF peaks, demonstrating γ-rays' ability to create an inorganic-rich SEI beyond what is achievable through conventional electrochemical methods.

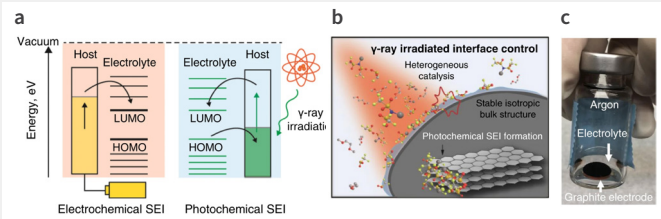

Fig. 1 Photochemical SEI formation induced by γ-rays. a Distinct energy schemes in the formation of the SEI using electrochemical and photochemical approaches. b Interface modification of the graphite electrode induced by γ-ray irradiation. c Photograph of the graphite electrode immersed in the electrolyte inside a vial filled with argon for γ-ray irradiation.

γ-Ray-induced photochemical SEI

The photochemical SEI formation allows testing under varied electrolyte conditions without standard electrolyte constraints, as demonstrated by immersing graphite electrodes in electrolytes and exposing them to γ-rays (Fig. 1c). The selection of 1 M lithium bis(trifluoromethanesulfonyl)imide (LiTFSI) in EC/DEC (50/50 v/v) was based on its superior rate performance and LiF content compared to other salts. X-ray diffraction (XRD) confirmed the graphite structure remained unchanged post-irradiation, indicating photolysis is interface-focused, supported by nuclear magnetic resonance (NMR) spectroscopy results.

Transmission electron microscopy (TEM) and energy dispersive spectroscopy (EDS) mapping showed a uniform ~20 nm photo-SEI layer on graphite, extending into particle pores, beneficial for fast Li-ion transport (Figs. 2a, b, c). Analysis on highly

oriented pyrolytic graphite (HOPG) showed a distinct photo-SEI composition with higher fluorine content compared to electrochemically formed SEI, highlighting the inorganic-rich nature of the photo-SEI layer (Fig. 2d, e, f).

Surface analysis of photo-HOPG showed increased hydrophilicity and an inorganic-rich interface confirmed by Raman spectroscopy and atomic force microscopy (AFM), demonstrating uniform LiF-rich SEI coverage (Fig. 3a, b, c, d, and Supplementary Fig. 14). This uniformity, challenging with rigid inorganic crystals, underscores the potential of γ-ray-induced photochemical processes in SEI formation.

Electrochemical tests on the photo-graphite cell

Electrochemical impedance spectroscopy showed that the photo-graphite cell's interfacial ionic resistance was significantly reduced after photochemical treatment, indicating a highly compact SEI layer and low resistance across lithiation potentials (Fig. 4a)[8][27]. Electrochemically, the photo-graphite cell retained the graphite's main Li storage behavior with less polarization even at low rates (Fig. 4b, 4c)[28].

Specific capacity tests revealed that the photo-graphite cell outperformed the bare cell at higher C-rates, retaining more capacity and showing distinct lithiation profiles with lower overpotentials, indicative of superior charging capabilities (Fig. 4d, 4e)[29]. In full cells with a NCM622 cathode, the photo-graphite showed enhanced charging performance and lower overpotentials (Fig. 5a, b). Under constant voltage, the photo-graphite cell demonstrated robust cycling for 300 cycles and resisted overcharging at high C-rates, unlike the bare cell which showed Li metal plating and fluctuating capacities (Fig. 5c).

The photo-graphite cell required less time to reach 80% state-of-charge (SOC) at higher C-rates, underscoring its fast charging capability (Fig. 5d)[8]. Long-term cycling at fast charging conditions was stable for the photo-graphite cell, with a high Coulombic efficiency, contrasting with the bare cell's capacity fluctuations and CE destabilization (Fig. 5e, 5f).

Microscopy showed the bare graphite electrode covered with Li plating after 100 cycles, while the photo-graphite electrode remained clean. The low interfacial resistance SEI enabled better low-temperature performance and higher temperature cycling for the photo-graphite. Post-mortem analysis showed a thicker SEI on the bare electrode, indicative of uncontrolled growth and Li plating, as opposed to the photo-graphite electrode (Fig. 6a).

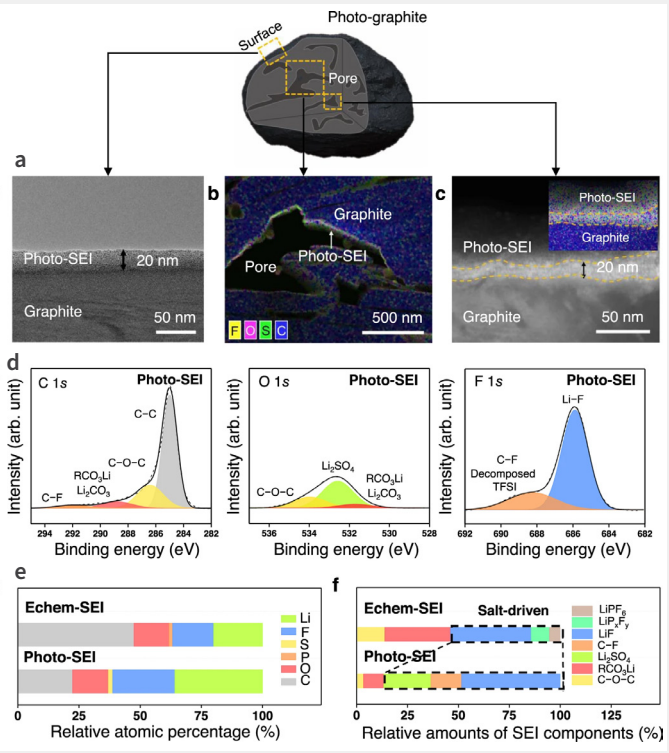

Fig. 2 Characterisation of the photo-SEI. a Cs-TEM image of the photo-graphite with the photochemically driven SEI layer. b Low-magnification EDS elemental map of the photo-SEI inside the pores of the photo-graphite electrode. c High-magnification Cs-TEM image of the photo-SEI image and the corresponding EDS map (inset). d XPS profiles of the photo-SEI in the C 1s (left), O 1s (middle) and F 1s (right) bands. e Relative atomic contents of echem- SEI and photo-SEI. f Relative amounts of SEI components in echem-SEI and photo-SEI. The photo-SEI in this figure originates from 1 M LiTFSI in EC/DEC (50/50 = v/v).

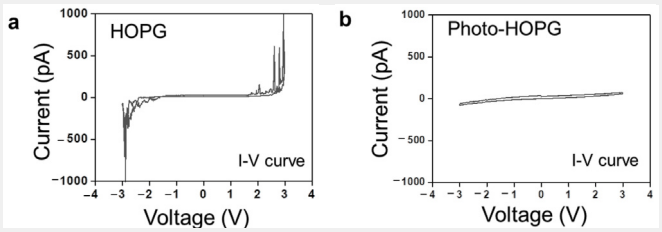

Supplementary Fig. 14. I-V curves of (a) the bare HOPG and (b) photo-HOPG using conductiev AFM

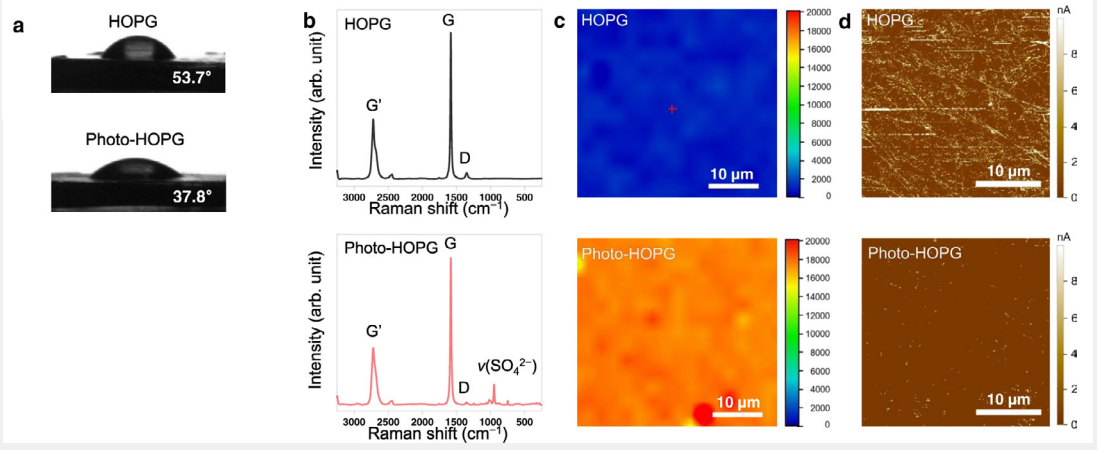

Fig. 3 Characterisation of bare and photo-HOPG. a Contact angle measurements of bare HOPG and photo-HOPG. b Raman spectra of bare HOPG and photo-HOPG. c Raman 2D mapping images of bare HOPG and photo-HOPG at 950 cm^{-1}. d AFM current mapping images of HOPG and photo-HOPG with 0.5 V bias.

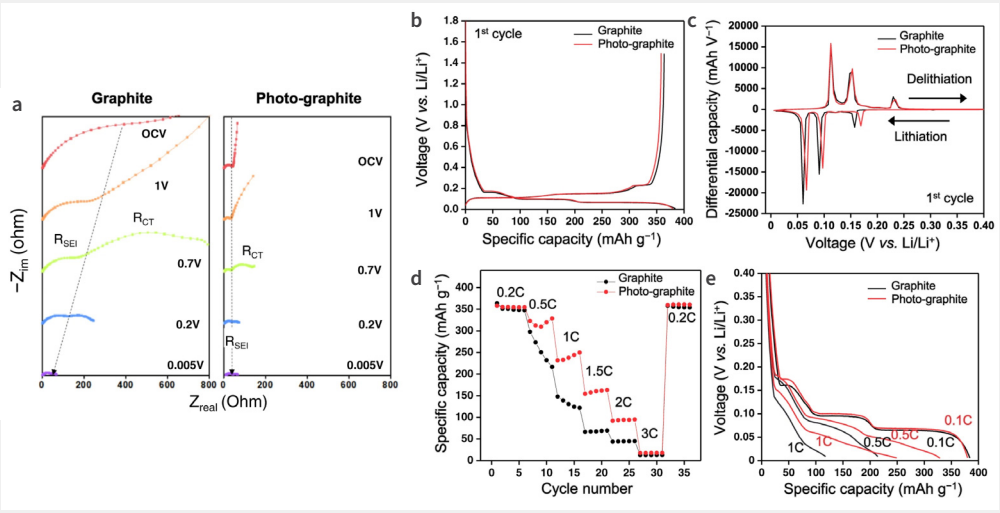

Fig. 4 Electrochemical measurement of graphite half-cells. a EIS profiles of bare graphite and photo-graphite half-cells during the initial cycles. b Initial charge and discharge profiles of bare graphite and photo-graphite half-cells when scanned at 0.1 C (35 mA g^{-1}). c dQ/dV profiles of bare graphite and photo-graphite half-cells during the initial cycles at 0.1 C (35 mA g^{-1}). d Rate capability results of bare graphite and photo-graphite half-cells. e Comparative discharge profiles at 0.1 C, 0.5 C and 1 C. The active material loading for these results was 8.3 mg cm^{-2}.

SEI composition, particularly the inorganic-to-organic content ratio, is crucial for preventing SEI growth, Li metal plating, and ensuring fast charging with robust cycling (Fig. 6b). An inorganic-rich SEI is insulating and prevents electron transfer, maintaining a thin layer that supports fast charging operations without parasitic reactions or overcharging[34][35][36].

DISCUSSION

The main challenge in achieving extremely fast charging (XFC) for lithium-ion batteries has been speeding up lithium ion movement at the electrode interface without reducing battery life or safety. Traditionally, there's been little control over how the materials in the electrolyte break down, which affects the battery's performance. However, this study introduces a method using ɣ-ray irradiation to selectively break down fluoride-containing salts, leading to a lithium fluoride (LiF)-rich solid-electrolyte interphase (SEI) layer. This new inorganic-rich SEI layer enhances lithium ion diffusion and maintains stability, thus supporting a longer battery life and allowing the battery to charge up to 80% in just 10.8 minutes. Although ɣ-ray techniques might not be ready for immediate use in existing battery production, they offer valuable strategies for improving electrolytes and could influence further research on enhancing the stability of lithium-ion battery interfaces.

METHODS

Materials:

Mesocarbon microbeads (MCMB) graphite for anodes and NCM622 for cathodes were used as active materials. Highly oriented pyrolytic graphite (HOPG) was acquired from Alfa Aesar. Lithium salts LiTFSI and LiFSI were purchased from Sigma-Aldrich, USA, and solvent N-methyl-2-pyrrolidone (NMP) was obtained from JUNSEI, Japan. The conductive agent Super P came from Timcal, Switzerland. The electrolyte comprised 1 M $LiPF_6$ in EC/DEC with 10 wt% FEC, sourced from Wellcos Corporation, South Korea. Binders used were SBR from Zeon and CMC from Sigma-Aldrich for graphite electrodes, and PVDF (Kynar) for NCM622 electrodes.

Physicochemical Characterization:

Atomic Force Microscopy (AFM) was conducted with the Park NX10 from Park Systems, South Korea, to map out

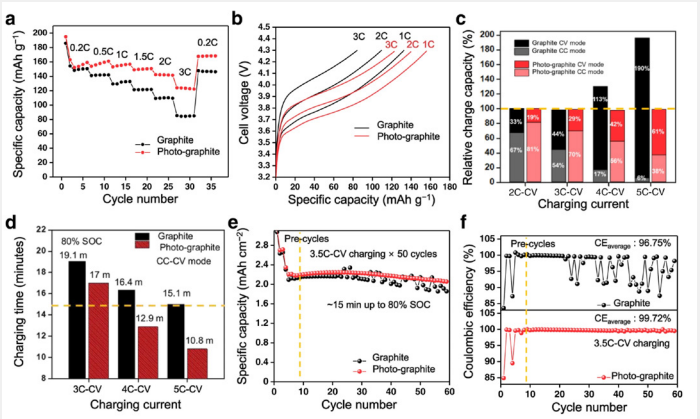

Fig. 5 Electrochemical measurements of photo-graphite full-cell. a Rate capability test results of bare graphite and photo-graphite full-cells. b Charging profile comparison at 1 C, 2 C and 3 C. c Relative charge capacity for CC and CV modes at various charging rates. d Charging time to reach the 80% SOC at various charging rates. e Cycling performance of both types of full-cells at 3.5 C in CC-CV mode. f Comparison of the Coulombic efficiency at 3.5 C in CC- CV mode. Both types of full-cells have an areal capacity of 2.6 mAh cm^{-2} and N/P ratio of 1.1.

the electronic conductivity by applying a voltage of 0.5 volts to the sample, at the RIAM of Seoul National University. XPS analysis utilized an AXIS-His spectrometer from KRATOS, U.K., and FE-SEM imaging was done using a JSM-7600F from JEOL, Japan. XRD patterns were captured with a Smart Lab from Rigaku, Japan, and cross-sections of photo-SEI were observed using a Cs-corrected TEM (JEM-ARM200F) from JEOL, Japan. Contact angles were measured with a DSA100 from Kruss, Germany, and Raman spectra were recorded using a RAMAN spectrometer II (DXR2xi) from Thermo Fisher, USA. LC–MS analysis was conducted with a Ultimate 3000 from Thermo Scientific, USA, using a Triple TOF 5600 from AB Sciex, USA. NMR used a 500 MHz AvanceIII-500 from Bruker, Germany, at NCIRF, Seoul National University, and FE-EPMA was performed on a JXA-8530F from JEOL, Japan.

Preparation of Electrodes:

For graphite electrodes, a slurry with graphite, Super P, and SBR-CMC binders was spread onto copper foil and dried at 60 °C in a vacuum. Cathodes comprised a slurry of NCM622, Super P, and PVDF cast onto aluminum foil. Photo-graphite electrodes were prepared by immersing them in 1 M LiTFSI in EC/DEC and irradiating with ɣ-rays from an MDS Nordion irradiator at the Korea Atomic Energy Research Institute, then cleaned with DEC.

Electrochemical Characterization:
CR2032 coin cells were assembled for electrochemical testing, which involved pre-cycling and resting the cells with an electrolyte and separator from SK Innovation, South Korea. The cells were cycled using a battery cycler (WBCS 3000) from Wonatech, South Korea, and EIS measurements were taken with a potentiostat (VSP) from Bio-Logic, France. The rate capability and cycling performance at various temperatures were also evaluated, employing cells with precisely measured capacities.

DATA AVAILABILITY

The data that support the findings of this study are available from the corresponding author upon reasonable request.

REFERENCES

For the list of references, please go to https://doi.org/10.1038/s41467-021-27095-w

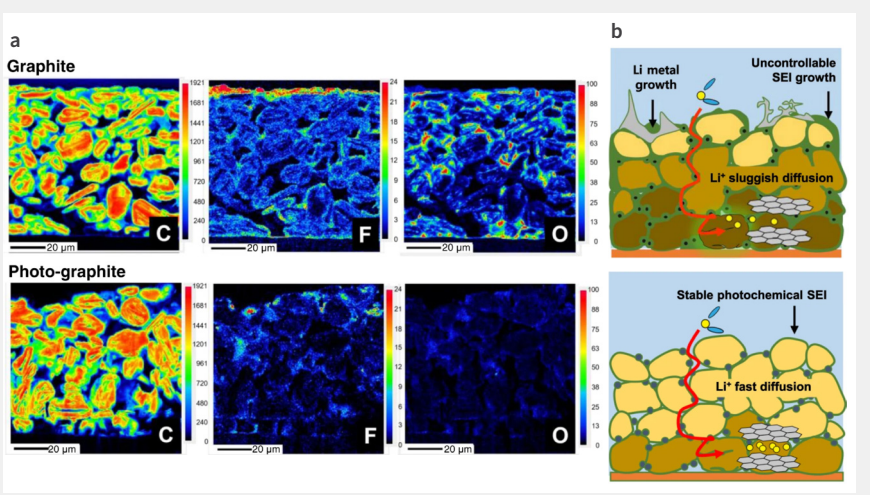

Fig. 6 Ex situ characterisation of both types of graphite electrodes. a FE-EPMA mapping images of cross-sections of bare graphite and photo-graphite after rate capability tests. b Schematic illustrations of problems expected with fast charging and the advantageous effect of the photochemical SEI.

News you might have missed...

PARK SYSTEMS CONTINUES ITS REIGN AS MARKET LEADER IN ATOMIC FORCE MICROSCOPY

20 March 2024

Park Systems, a leading manufacturer of nano-metrology systems, proudly maintains its position as the industry leader in the atomic force microscopy (AFM) market for the second consecutive year as of 2023, according to QY Research 2024. In an ever-competitive landscape, Park Systems has once again outpaced its competitors by securing the top spot in market share of 20.61% in 2023, demonstrating unwavering excellence and commitment to advancing AFM technology.

The QY Research report reveals that the global AFM market was valued at USD $485.44 million in 2023, with projections to soar to USD $1013.58 million by the end of 2030, growing at a compound annual growth rate (CAGR) of 10.92% during 2024-2030. From 2019 to 2023, Park Systems has demonstrated an impressive CAGR of 30%, markedly higher than its main competitors, according to QY Research. While major competitors have grown with CAGRs of approximately 8% and 10% respectively, Park Systems has outpaced the competition with a staggering CAGR.

The strategic acquisition of Accurion GmbH, a Germany-based company known for its imaging spectroscopic ellipsometers (ISE) and active vibration isolations (AVI), marks a pivotal step in Park Systems's strategy to broaden its technology portfolio and cement its market dominance. This move not only diversifies Park Systems's offerings but also enhances its capabilities to cater to a broader array of scientific and industrial nano-metrology applications with unmatched precision and innovation.

"The latest QY Research report affirms our lead in the AFM market and highlights our drive for innovation. With Accurion GmbH joining our ranks, we continue to push technological boundaries and address our customers' growing needs," said Dr. Sang-Joon Cho, Executive VP of Sales at Park Systems.

The extensive presence of Park Systems across North America, Europe, and Asia-Pacific, supported by a comprehensive network of support centers, ensures that it remains at the forefront of customer service and technological advancement. This global footprint allows Park Systems to effectively address the needs of its diverse customer base, reinforcing its market leadership and commitment to excellence.

Looking ahead, Park Systems is committed to ongoing innovation and the exploration of new applications for AFM technology. The company aims to continue expanding its product offerings and enhancing its technology to meet the growing needs of nano-metrology for scientific and industrial markets.

Announcement

THE 2024 NANOSCIENTIFIC SYMPOSIUMS ARE SCHEDULED FOR KEY GLOBAL REGIONS

Park Systems is pleased to announce the 2024 schedule for the NanoScientific Symposiums. These renowned events are set to take place across major global regions, including SE Asia, China, Japan, Europe the Americas, and Korea.

Following their successful run of both virtual and live events in previous years, the symposiums have historically united thousands of international attendees across five continents, promoting rich discussions and collaborations in the field of nanoscience. The 2024 symposiums will continue this tradition, offering participants the opportunity to present their research and compete for prizes in both presentations and poster exhibits.

The symposiums are scheduled as follows:

- SE Asia: Chulalongkorn University, Bangkok, Thailand, August 6.
- China: SINANO Chinese Academy of Sciences, Suzhou, September 21-22.
- Japan: Tokyo Institute of Technology, October 18.
- Europe: Fraunhofer EMFT, Munich, Germany, October 29-31.
- Americas: Arizona State University, Phoenix, Arizona, November 13-14.
- Korea: Paradise Hotel, Busan, November 21.

Each event will cover a broad spectrum of topics such as electrical properties in semiconductors, 2D materials, surface science, and molecular biology, with a special emphasis on the practical applications of nanoscience in both industry and academia.

Park Systems invites researchers from around the world to submit their papers and posters for consideration. Prizes will be awarded for outstanding presentations, providing further incentives for contributors to share their innovative findings. Please mark your calendar for the symposium in your region.

For more information on each regional symposium, including registration for each location, visit nanoscientific.org/nss2024. Updates on the symposium topics, keynote speakers, and other event details will be progressively announced on the website.

ICCAS 2024

THE INTERNATIONAL CONFERENCE ON CONTROL, AUTOMATION AND SYSTEMS

The 24th International Conference on Control, Automation and Systems

October 29(Tue)~ November 1 (Fri), 2024

Jeju Shinhwa World, Jeju, Korea

General Chair
Sang-il Park — Park Systems

General Co-Chair
PooGyeon Park — POSTECH

Program Chairs
Jaeheung Park — Seoul National University
Yongsoon Eun — DGIST

Invited Session Chairs
Young Soo Suh — University of Ulsan
Hyungbo Shim — Seoul National University
Dongjun Lee — Seoul National University
Hyun Myung — KAIST
Chang-Sei Kim — Chonnam National University
Jongeun Choi — Yonsei University
Sehoon Oh — DGIST
Choon Ki Ahn — Korea University
Jong Min Lee — Seoul National University
Yoonsoo Kim — Gyeongsang National University
Sung Hyun Kim — University of Ulsan
Jaewook Shin — Kumoh National Institute of Technology

Student Activity Chairs
Soohee Han — POSTECH
Cheolhyeon Kwon — UNIST

International Relation Chairs
Jun Moon — Hanyang University
Jinoh Lee — DLR German Aerospace Center
Jian Sun — Beijing Institute of Technology
Toru Namerikawa — Keio University
David Banjerdpongchai — Chulalongkorn University

Workshop & Tutorials Chairs
Juhoon Back — Kwangwoon University
Jung-Su kim — SeoulTech

Publication Chairs
Bum Yong Park — Kumoh National Institute of Technology
Sangmoon Lee — Kyungpook National University

Publicity Chairs
Hyo-Sung Ahn — GIST
Pyojin Kim — GIST

Industry Chairs
Young-Jin Lee — ROBONE
Kyoung-Chul Koh — Koh Young Technology
Jay Lee — Mathworks Korea
Doo Jin Choi — Samsung Heavy Industries
Jae Won Lee — Suprema

Exhibition Chairs
Jung Hoon Kim — POSTECH
Chaneun Park — Kyungpook National University

Local Arrangement Chairs
Ho-Chan Kim — Jeju National University
Seongmin Lee — Jeju National University

Award Chairs
Nak Yong Ko — Chosun University
Hye-Kyung Cho — Hansung University
Tae-Hyoung Park — Chungbuk National University
Kyoung-kwan Ahn — University of Ulsan
Hyoun Jin Kim — Seoul National University

Contact

TEL +82-2-6949-5801 (ext.3)
FAX +82-2-6949-5807
E-mail conference@icros.org

Plenary Speakers

Dongil "Dan" Cho
Seoul Nat'l Univ., Korea

Florian Dorfler
Swiss Federal Inst. of Tech., Switzerland

Lei Guo
Beihang University, China

Yoshito Ohta
Kyoto University, Japan

Jan Peters
TU Darmstadt, Germany

Topic

- > Control Theory and Applications
- > Control Devices and Instruments
- > Industrial Applications of Control
- > Sensors and Signal Processing
- > Artificial Intelligent Systems
- > Robot Mechanism and Control
- > Robot Vision
- > Human-Robot Interaction
- > Exoskeletal Robot
- > Robotic Applications
- > Autonomous Vehicle Systems
- > Navigation, Guidance and Control
- > Process Control Systems
- > Biomedical Instruments and Systems
- > Information and Networking
- > Multimedia Systems
- > Civil and Urban Control Systems
- > Rehabilitation Robot

Important Dates

May	**1, 2024**	Submission of organized session proposals
May	**31, 2024**	Submission of full papers
July	**31, 2024**	Notification of paper acceptance
August	**31, 2024**	Submission of final camera-ready papers

Paper Submission

You are cordially invited to submit papers to https://2024.iccas.org. Paper template file can be downloaded from the website. *Accepted papers will be submitted for inclusion into IEEE Xplore subject to meeting IEEE Xplore's scope and quality requirements. And it will be published in the ICCAS 2024 Proceedings*, SCOPUS and EI compendex, and will be submitted for indexing in Clarivate Analytics Conference Proceedings Citation Index (Web of Science).

Organized by

the Institute of Control, Robotics and Systems (ICROS)

Technically Co-Sponsored by

IEEE · ACA · SCE · CAA · AAI · ISA · CAC · ECTI Association

https://2024.iccas.org/

NANOscientific Symposium 2024

REGISTER NOW!

nanoscientific.org/nss2024

The 2024 NANOscientific Symposium is set to be a landmark event, uniting global experts in the fields of nanoscience and nanotechnology. This year, we extend our focus beyond Scanning Probe Microscopy (SPM) to encompass a broader range of nanotechnological applications and innovations. With an enriched agenda featuring keynote presentations from trailblazers in the industry, interactive sessions, and enhanced virtual networking opportunities, attendees will have unprecedented access to resources and collaborations that drive research, innovation, and commercial success in the ever-evolving world of nanotechnology.

NSS Americas
13 - 14 Nov | Phoenix, USA

NSS China
21 - 22 Sep | Suzhou, China

NSF Europe
29 - 31 Oct | Munich, Germany

NSS Japan
18 Oct | Tokyo, Japan

NSS Asia
02 Aug | Bangkok, Thailand

NSS Korea
21 Nov | Busan, Korea

Sponsored By

Park SYSTEMS

NANOTECHNOLOGY WORLD ASSOCIATION